ČESKÉ VYSOKÉ UČENÍ TECHNICKÉ V PRAZE

Fakulta elektrotechnická

Diplomová práce

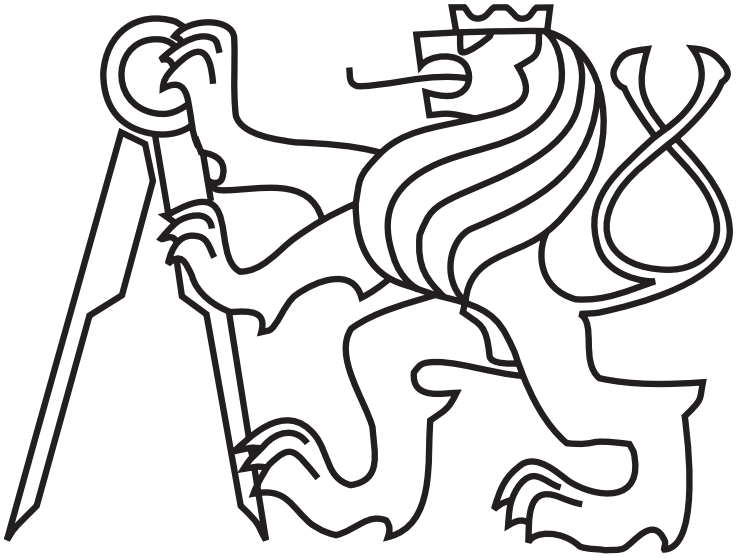

Bc. David Vojna

Numerická simulace šíření laserového svazku tepelně zatíženým prostředím

Katedra řídicí techniky

Vedoucí diplomové práce: **Ing. Ondřej Slezák, Ph.D.**

České vysoké učení technické v Praze
Fakulta elektrotechnická

katedra řídicí techniky

ZADÁNÍ DIPLOMOVÉ PRÁCE

Student: **Bc. David Vojna**

Studijní program: Kybernetika a robotika
Obor: Systémy a řízení

Název tématu: **Numerická simulace šíření laserového svazku tepelně zatíženým prostředím**

Pokyny pro vypracování:

1. Navrhněte a implementujte algoritmus pro výpočet trajektorie laserového svazku v obecném 2D diskretizovaném optickém prostředí s možností rozšíření na tepelně zatížené optické prvky v prostředí MATLAB.
2. Popište deformované výpočetní sítě metody konečných prvků pro tepelně zatížené optické prvky a implementujte jejich převod do prostředí MATLAB pro použití v navrhovaném algoritmu.
3. Ověřte funkčnost algoritmu jeho využitím pro analýzu šíření laserového svazku v některých jednoduchých optických prvcích užívaných pro řízení šíření svazku v laserových systémech.

Seznam odborné literatury:

[1] Schrader, K. N., Subia, S. R., Myre, J. W., and Summers, K. L., Ray tracing in a finite-element domain using nodal basis functions, Appl. Opt. 53, F10-F20, (2014).
[2] Rahman, B. M. A., and Agrawal, A., Finite Element Modeling Method for Photonics, Artech House, 2nd edition, (2013).
[3] Koechner, W., Solid State Laser Engeneering, Springer Science & Bussiness media, 6th edition, (2006).

Vedoucí: Ing. Ondřej Slezák, Ph.D.

Platnost zadání: do konce letního semestru 2016/2017

L.S.

prof. Ing. Michael Šebek, DrSc.
vedoucí katedry

prof. Ing. Pavel Ripka, CSc.
děkan

V Praze dne 3. 3. 2016

Prohlášení autora práce

Prohlašuji, že jsem předloženou práci vypracoval samostatně a že jsem uvedl veškeré použité informační zdroje v souladu s Metodickým pokynem o dodržování etických principů při přípravě vysokoškolských závěrečných prací.

V Praze dne ....

Podpis autora práce

Poděkování

Rád bych zde poděkoval vedoucímu této práce, Ing. Ondřeji Slezákovi, Ph.D., za ochotu, cenné rady a metodické vedení této práce. Dále děkuji své rodině, přátelům a především své přítelkyni za podporu, toleranci a chvíle rozptýlení.

Abstract

This work deals with numerical simulations of a laser beam propagation through a thermally loaded solid-state 2D medium. At first a brief introduction to basic principles of laser physics is given followed by a simplified description of thermo-optic effects associated with laser system operation. Finite element methodology is presented as a practical tool for thermo-mechanical analysis of two dimensional models of system optical elements. A procedure is developed to integrate the FEM analysis results and computational mesh in a numerical algorithm simulating the laser beam propagation. Laser beam is approximated as a set of rays within this work. The algorithm performance is validated for both homogeneous and graded-index media using comparison method of numerical and analytical solutions. An example of thermo-optical analysis of a zigzag laser amplifier is also included.

Abstrakt

Tato práce se zabývá numerickými simulacemi šíření laserového svazku tepelně zatíženým 2D prostředím. Nejprve jsou stručně uvedeny základní principy laserové fyziky následovány zjednodušeným popisem tepelně-optických jevů spojené s provozem pevnolátkových laserových systémů. Metoda konečných prvků je prezentována jako praktický nátroj pro tepelně mechanickou analýzu optických prvků systému. Je vyvinut postup pro integraci výsledků analýzy a výpočetní sítě metody konečných prvků v numerickém algoritmu simulujícím šíření laserového svazku. Laserový svazek je v této práci aproximován skupinou paprsků. Funkčnost algoritmu je ověřena pro homogenní i gradientní prostředí metodou porovnání numerického a analytického řešení. Práce zahrnuje i příklad tepelně optické analýzy laserového zigzag zesilovače.

Contents

Chapter 1

Introduction

This diploma thesis deals with numerical simulations of a laser beam propagation through a thermally loaded solid-state media. Numerical simulations represents an essential part of development cycle of optical devices. The cycle covers design, fabrication, characterization as well as possible redesign. The role of computerized modelling and simulation tools is important in reducing the time and costs involved in this cycle. The core contribution of the thesis is design and implementation of a numerical algorithm for simulation of a laser beam propagation in optical components commonly used in solid-state laser systems. Since the task is generally non-trial, many simplifications were made within the scope of this work. Among the most significant ones is a restriction to only two dimensional problems and consideration of a laser beam as of a set of rays. Most widely used optical components such as lenses, windows or laser crystals meets criteria for the ray approximation.
The thesis starts with a brief introduction to basic principles of laser physics. Laser light generation based on optical amplification of radiation in interaction with matter is described as well as the principle parts of an operational laser device. Possible ways of categorization of laser systems according to their parameters is also included. Since the laser devices are nowadays used in a vast number of multidisciplinary applications, their concise laser overview is given at the end of the first introductory chapter.
Solid-state laser system operation is often limited by thermo-optic effects arisen due to parasitic heat generation in all optical components within the system. These effects represents one of key limiting factors of laser system operation especially when considering high average powers. A simplified overview of causes and the resulting effects is presented in the third chapter along with a set of model equations and formulas mainly used for thermo-optical analysis. The set mainly consists of partial differential equations for which obtaining the analytical solution is for most of practical cases very tedious or even impossible.
Widely used finite element methodology is shortly presented in the forth chapter as a practical tool to deal with such a set of partial differential equations. The main idea of the method is described followed by the main steps in the method implementation. More detailed description of 2D computational meshes and the shape functions is given since they play a key role in development of the numerical algorithm.
The next chapter is dedicated to the numerical algorithm design. A procedure is built to solve the differential ray equation within a discretized 2D finite element domain. The algorithm validity and its performance is then subjected to a detailed investigation. Numerical results of obtained ray trajectories for both homogeneous and gradient refractive index me-

dia are presented and compared with derived closed-form solutions. A full thermo-optical analysis is showed on an illustratory example of wavefront distortions examination in a laser amplifier with a zigzag geometry.
The thesis is concluded in the final chapter with the most important presented results and observations as well as with possible future improvements of this work that still needs to be done.

Chapter 2

Principles of Laser

Laser physics is an interdisciplinary scientific field containing apart from optics also photonics, quantum electronics, semiconductor and solid-state physics and many others ([1]). Hence the laser physics represents a very extensive topic. The goal of this introductory chapter is certainly not to fully describe the whole problematic but to give at least a rough introduction to key principles of laser light generation, basic scheme of an operational laser device as well as possible ways of laser systems classification and applications. For more detailed information one can search among vast number of great literature (i. e. [1] - [4]).

2.1 Laser light generation

The key principles of laser light generation stands on interaction of radiation with matter. Matter may be approximated as an atomic systems consisting of a large number of atoms, ions or moleculs which can exists only in discrete energy states. Transition between the two energy states is associated with either emission or absorption of a portion of radiation. The figure 2.1 depicts transition processes between two discrete energy levels E_2 and E_1. The frequency f_{21} of the radiation associated with transition between higher energy state E_2 and lower energy state E_1 can be expressed as follows ([1], [2])

$$E_2 - E_1 = hf_{21} \quad , \tag{2.1}$$

where h is the Planck's constant. Electromagnetic waves with the frequency f_{21} correspond-

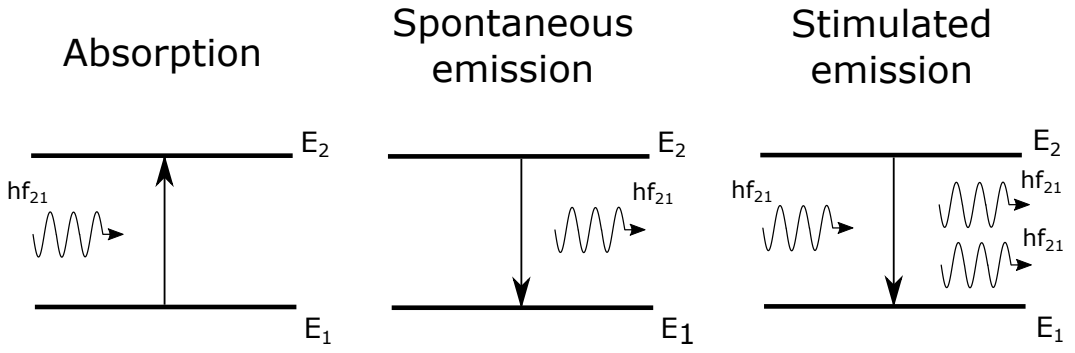

Figure 2.1: Transition processes between two discrete energy levels E_2 and E_1.

ing to an energy difference according to the equation (2.1) can interact with such atomic system. At thermal equilibrium, the lower energy levels of a atomic system are more heavily populated than the higher energy states. A wave interacting with the substance will in this case raise the atoms from lower energy state to the higher one and thereby experiencing absorption ([2]). The requirement of the laser operation is that the higher energy level is more heavily populated than the lower energy level. Such a state may be achieved by an external energy source. Absorption of the energy from the external energy source causes population inversion enabling the laser operation.
An electromagnetic wave of appropriate frequency, incident on the material with population inversion, will be amplified as the incident photons cause the higher energy atoms to drop to a lower level and emit additional photons. As a result, energy is extracted from the atomic system and supplied to the radiation field. The release of the stored energy by interaction with an electromagnetic wave is based on stimulated emission. After all, the acronym laser stands for Light Amplification by Stimulated Emission of Radiation.
The stimulated emission has the same directional properties, same polarization, phase and spectral characteristic as the stimulating radiation. As a consequence the degree of coherence of laser emission can be really high.

2.2 Principal parts of a laser device

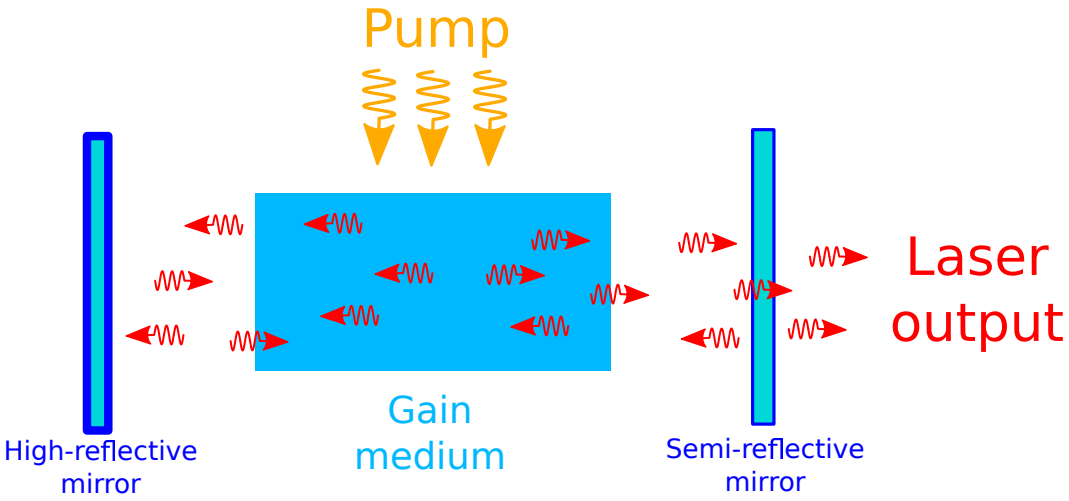

Figure 2.2: Simplified scheme of an optical resonator with two parallel mirrors placed around the gain medium and transversal pumping.

An operational laser device consists of three principal parts. Those parts are the gain medium, the pump, the optical resonator. Usually another essential part represents a cooling device.
The gain medium refers to a material in which the population inversion is created using the external energy source which is called the pump. The type of the pump source can be various as well as the material of the gain medium. Selection of the gain medium eventually determines the wavelength of the laser emission.
The optical resonator concentrates the light into the gain medium to stimulate the emission

of laser radiation. The figure 2.2 shows a simplified scheme of optical resonator formed by two parallel mirrors placed around the gain medium. In such configuration one of the mirrors is typically high-reflective for a radiation with laser emission wavelength, whereas the second mirror is typically semi-reflective. Both mirrors reflect the generated laser radiation back to the gain medium providing positive feedback. The semi-reflective mirror also transmits a part of the incident laser radiation out of the resonator forming the laser output.

2.3 Classification of laser systems

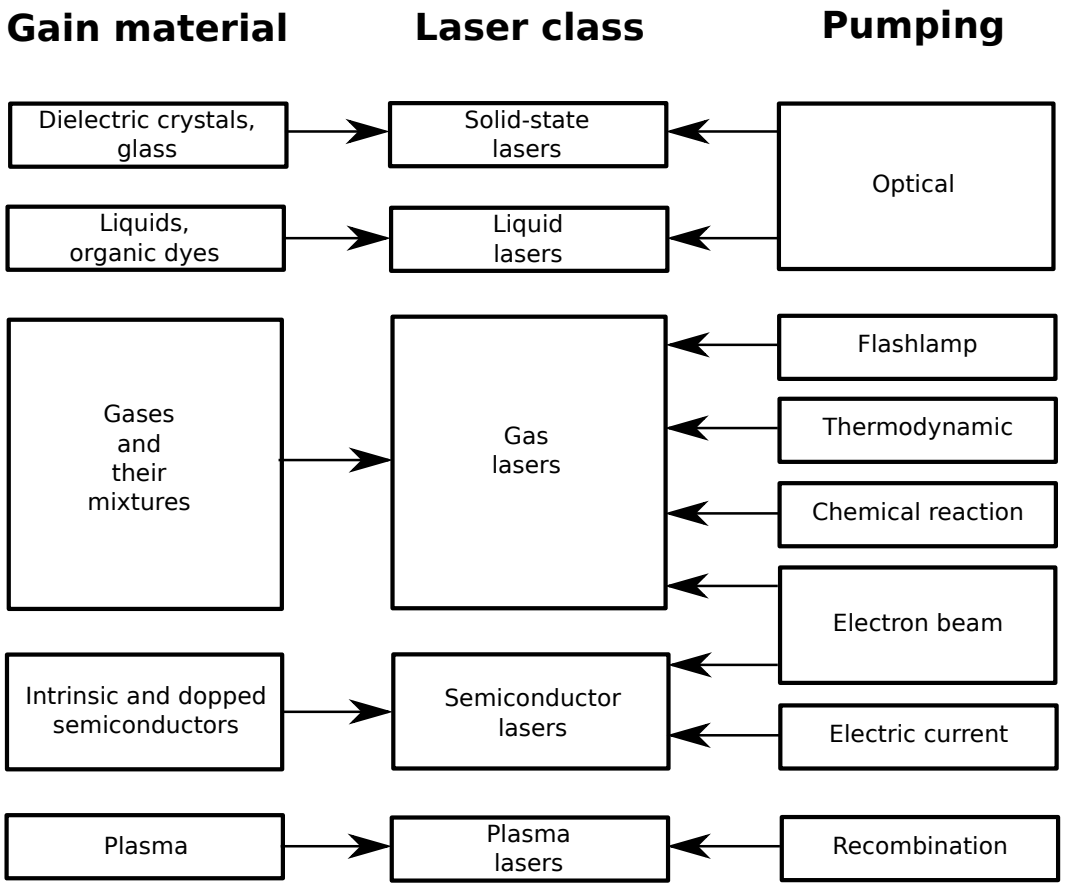

Figure 2.3: Classification of lasers ([1]).

Laser systems may be classified according to many different parameters. We may categorize lasers according to i. e. used gain medium, wavelength of the laser beam, type of the pump or the operation mode of the laser ([1]). Scheme of such categorization is given in the figure 2.3. With respect to the gain medium we may distinguish

- Solid-state lasers,
- Semiconductor lasers,
- Gas lasers,
- Liquid lasers,

- Plasma lasers.

According to the wavelength of the laser beam classification we differentiate

- Infrared lasers,
- Visible-light lasers,
- Ultraviolet lasers,
- X-ray lasers.

With respect to most commonly used types of the pump source let us mention

- Optically-pumped lasers (i.e. Flashlamp-pumped),
- Lasers pumped by a thermodynamic change of the gain medium,
- Chemical reaction pumping,
- Recombination,
- Electrical current or electron beam pumping,

And finally, we may operate the laser in following three modes

- Single-shot,
- Pulsed,
- Continuous wave.

2.4 Laser applications

Ever since the first operational laser was built in 1960 there has been a huge growth of interest in lasers. Highly collimated, monochromatic and coherence properties of a laser beam has been found useful in multitude of scientific, industrial, medical, military and commercial applications ([1], [5]). Among scientific laser applications should be mentioned

- Laser spectroscopy,
- Microscopy,
- Interferometry,
- Nuclear fusion.

In medicine field lasers are used for example in

- Ophthalmology for eye surgeries or diagnostics,
- Dentistry to remove carries,

- Dermatology for cosmetic surgeries or tissue bio-stimulation.

Military applications of laser cover

- Guidance and targeting of missiles,
- Laser sight for weapons,
- Navigation and location of aircraft.

From industrial applications we should point out mainly

- Cutting, welding, drilling and marking of materials,
- Amplifiers for optical systems in telecommunication,
- Optical devices in information technologies.

Above mentioned applications are just a few of a vast number used nowadays and more and more are being found with the technology development.

Chapter 3

Thermo-optic effects in solid-state laser systems

Solid-state laser system operation is limited by thermo-optic effects arisen due to parasitic heat generation in all optical materials including active laser medium. Efficient heat removal and the reduction of the thermal effects that are caused by the temperature gradients across the active area of optical elements has to be considered during design of high average power laser systems ([2], [6] - [12], [15]).

3.1 Thermo-optic effects

The optical pumping in a solid-state laser material is associated with the heat generation for a number of reasons among the most significant ones are ([2]) :

- The energy difference of the photons between the pump band and the upper laser level is lost as heat to the host material. Similarly, the energy difference between the lower laser level and the ground state is also changed into heat. The difference between the pump and the laser photon energies is the major source of heating in solid-state lasers and is called quantum defect.
- Nonradiative relaxation from the upper laser level to the ground state and nonradiative relaxation from the pump band to the ground state will generate heat in active medium because of concentration quenching.
- In flashlamp-pumped systems, the broad spectral distribution of the pump source causes a certain amout of background absorption by the host laser material, particularly in the ultraviolet and infrared regions of the lamp spectrum. Absorption of lamp radiation by impurity atoms can further increase heating.

the generated temperature gradients as a result of absorption and non-uniform heat removal lead to various thermo-optic effects. Inhomogeneous temperature field induce inhomogeneous refractive index distribution in the material as well as thermal deformations caused by thermal stress. Further, the stress might even lead to fracture of the material. Below the stress fracture, thermal lensing and induced birefringence adversely affect the output beam

quality ([8] - [11]). Also, because of thermal lensing, the stable operating point of the laser resonator varies with the input power. Full description of all thermo-optic effects is certainly worth several books and is behind the scope of this work. Summarizing scheme of causes and resulting thermo-optic effects is given in the figure 3.1 to get the general idea. For more information see ([2], [6] - [12], [15]).

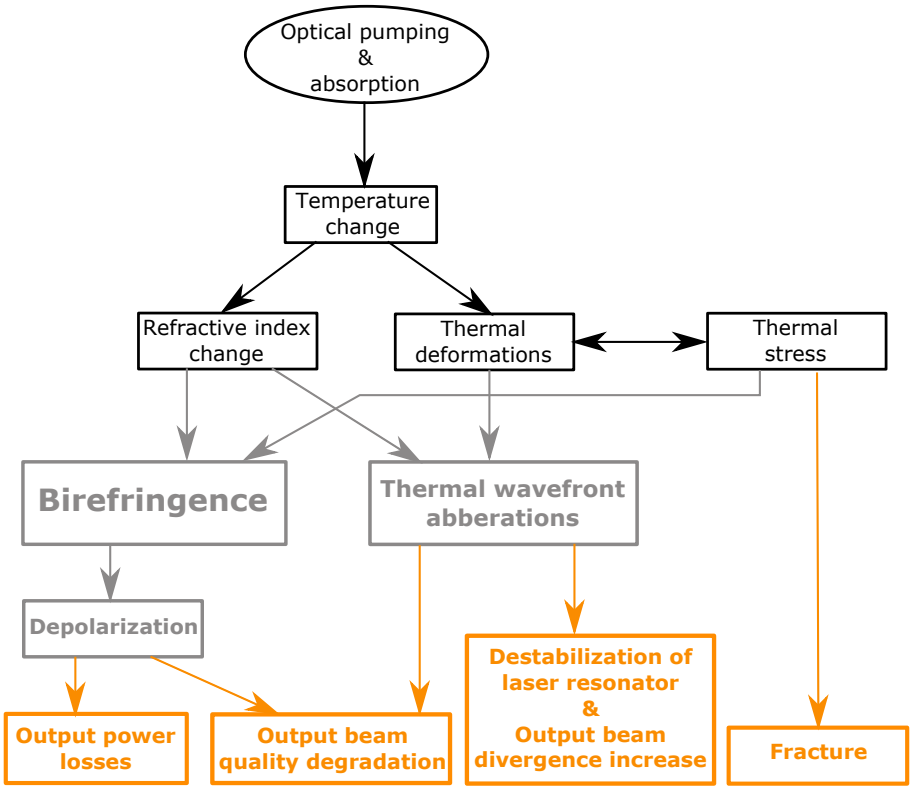

Figure 3.1: Summarizing scheme of causes and resulting thermo-optic effects.

3.2 Set of model equations and formulas for thermo-optical analysis

Even considering simplified scheme depicted in the figure 3.1, thermo-optical analysis is still quite complex. To obtain solution for the temperature field, arisen thermal stress and induced thermal deformations within the thermally loaded medium one needs to solve set of partial differential equations. This section is dedicated to presenting set of the main model equations used for thermo-optical analysis.

3.2.1 Heat transfer equation

The temperature field $T(\mathbf{r}, t)$ in thermally loaded isotropic medium is given by the heat transfer equation ([13])

$$\rho C_p \frac{\partial T(\mathbf{r}, t)}{\partial t} = \nabla \left[k \nabla T(\mathbf{r}, t) \right] + Q(\mathbf{r}, t) \quad , \tag{3.1}$$

where $\mathbf{r}$ is the position vector, t is the time, ρ stands for the material density, C_p is the specific heat at constant pressure, k is the thermal conductivity and $Q(\mathbf{r},t)$ is the heat source density. Assuming the steady-state approximation, the temporal dependence of the temperature vanishes and equation (3.1) becomes

$$-Q(\mathbf{r},t) = \nabla\left[k\nabla T(\mathbf{r},t)\right] \quad . \tag{3.2}$$

It should be noted that material parameters thermal conductivity $k(\mathbf{r},T)$, density $\rho(\mathbf{r},T)$ and specific heat $C_p(\mathbf{r},T)$ are in general temperature and spatial dependent. Spatial dependence refers to potential material inhomogeneities. Within this work these dependencies will not be considered.

3.2.2 Thermal stress equations

Change of the temperature in the medium leads to thermal expansion of the material. Together with the inhomogeneity of temperature field the thermal expansion results in arisen thermal stress which may be for the particular case of isotropic material calculated using following set of equations ([14],[15])

$$\frac{\partial \sigma_{ij}}{\partial x_j} + f_i = 0 \quad , \tag{3.3}$$

$$\sigma_{ij} = \delta_{ij}\lambda\epsilon_{kk} + 2\mu\epsilon_{ij} - \delta_{ij}(3\lambda + 2\mu)\alpha_T \quad , \tag{3.4}$$

$$\epsilon_{ij} = \frac{1}{2}\left(\frac{\partial u_i}{\partial x_j} + \frac{\partial u_j}{\partial x_i}\right) \quad , \tag{3.5}$$

where δ_{ij} stands for the Kronecker symbol, σ_{ij} denotes the stress tensor, f_i stands for the internal force, ϵ_{ij} is the strain tensor, α_T is the thermal expansion coefficient and u_i stands for displacement vector. Coefficients λ and μ are given

$$\lambda = \frac{\nu E}{(1+\nu)(1-2\nu)} \quad , \tag{3.6}$$

$$\mu = \frac{E}{2(1+\nu)} \quad , \tag{3.7}$$

where ν is the Poisson's ration and E stands for the Young's Modulus.
Set of equations (3.3) represents equilibrium conditions for the isotropic medium, followed by Duhamel-Hook's law in equation (3.4) relating stress and strain tensor components. The last set of equations (3.5) relates strain tensor components with the displacement field.

3.2.3 Refractive index variation

Steady-state inhomogeneous temperature distribution $T(\mathbf{r})$ together with induced thermal deformations in an active laser material results in inhomogeneous refractive index distribution expressed as follows

$$n(\mathbf{r}) = n_0 + \Delta n_T(\mathbf{r}) + \Delta n_S(\mathbf{r}) \quad , \tag{3.8}$$

where n_0 is the refractive index corresponding to the state of the medium before heating. The second term on the right hand of equation (3.8) represents temperature dependent change

of refractive index and its linear approximation may be experessed as follows ([2], [7], [15])

$$\Delta n(\mathbf{r})|_T = \frac{dn}{dT}\left[T(\mathbf{r}) - T_0\right], \tag{3.9}$$

where dn/dT is termed as the thermo-optic coefficient and is a material parameter.
The second term $\Delta n(\mathbf{r})|_S$ on the right hand of equation (3.8) represents the stress dependent change of the refractive index. The refractive index of a crystal is specified by the indicatrix, which is an ellipsoid whose coefficients are components of the relative dielectric impermeability tensor B_{ij}. A change of refractive index produced by stress is given by a small changes in shape, size and orientation of the indicatrix ([6]). The change is specified by the small changes in the coefficients B_{ij}. Neglecting the electro-optic effect, the changes ΔB_{ij} are given by

$$\Delta B_{ij} = p_{ijkl}\epsilon_{kl} \quad (i,j,k,l = 1,2,3) \quad , \tag{3.10}$$

where p_{ijkl} is a forth rank tensor giving the photo-elastic effect. The element of this tensor are the elasto-optic coefficients. ϵ_{kl} is a second rank strain tensor. Following steps of derivation of the stress induced change of refractive index are dependent on the vast amount of additional parameters (i. e. crystal orientation, crystallographic class of the particular material and light polarization). Because of this fact, let us express it generally as a function of ΔB_{ij} without going into a further detail as

$$\Delta n(\mathbf{r})|_S = f(\Delta B_{ij}) \quad . \tag{3.11}$$

In addition, compared to $\Delta n(\mathbf{r})|_T$ is the stress dependent change of refractive index $\Delta n(\mathbf{r})|_S$ relatively small and is often neglected for the sake of simplicity ([6]).

3.2.4 Equation for modelling of beam propagation through thermally loaded medium

To analyse the trajectory of a laser beam propagating through inhomogeneous refractive index media one have to choose proper laser beam approximation. Careful consideration of validity of the chosen approximation for the particular goal is always essential.
Considering the fact that the vast majority of the optical elements in solid-state laser systems meets the criteria for ray-optics approximation[1] it is often beneficial to approach to a laser beam rather as to a set of rays than to a wave. One of the main benefits of such choice is solving relatively less complicated differential equation compared to solving of the wave equation. The path of rays in a general graded-index medium is obtained by solving differential ray equation ([3])

$$\frac{d}{ds}\left[n(\mathbf{r})\frac{d\mathbf{r}}{ds}\right] = \nabla n(\mathbf{r}) \quad , \tag{3.12}$$

where $\mathbf{r}$ is the position vector of a point on the ray, $n(\mathbf{r})$ is the refractive index distribution in the medium and ds is a infinitesimal element of the arc length along the ray.

[1] Since most of the component are significantly larger than the wavelength of particular laser beam. One of exceptional case would be analysing beam propagation in optical fibers which will not be considered within this work.

Ray-optics approach enables analysis of major thermo-optic effects related to operation of solid-state laser systems such as wavefront distortions, thermal optical path differences or thermally induced depolarization (see [8]). The wave approach is essential and beneficial in cases that are beyond the scope of this work. Such case might be for example investigation of thermo-optic effects in optical fibers which do not exactly meet the criteria for ray-optics approximation. Another example might be frequency domain analysis of a laser beam propagation.

3.2.5 Change of the optical path

The optical path length of a ray propagating through a medium is defined as ([3])

$$OP = \int_L n(\mathbf{r}) ds \quad , \tag{3.13}$$

where L is the total distance travelled through the medium. The inhomogeneous temperature field in the medium and the corresponding mechanical stresses and strains cause the refractive index to vary from point to point and change its shape. These factors results in different optical path

$$OP_{new} = \int_{L_{new}} n(\mathbf{r}) ds \quad . \tag{3.14}$$

The optical path difference can be expressed as

$$OPD = OP_0 - OP_{new} = n_0 L_0 - \int_{L_{new}} n(\mathbf{r}) ds \quad , \tag{3.15}$$

where the index 0 refers to the state of non-heated medium. The change of the optical path of particular rays eventually leads to wavefront distortions of laser beam.

Chapter 4

Finite element methodology

Finite element methods are numerical methods for solving partial differential equations problems. The versatility of the method and the ability to produce robust, accurate results for challenging problems have led to its application in many branches of science and engineering ([16], [17]). The main concept of using finite elements for discretizing a structure is introduced in this section. A flowchart showing the main steps of the finite element method is presented and basic overview of meshing and shape functions is given.

4.1 The main concept of FEM

The repetitive nature of steps involved in FEM calculations makes the method suitable for computer implementation for large problem domains. The finite element methodology primarily involves ([16], [17])

- Representing the structure of interest as a patchwork of smaller elements.
- Expressing the unknown solution by an interpolation of values at nodes of the elements.
- Assembling the resulting equations for each element into global matrix equations.
- Solving the global system of equations.

The main concept of FEM lies in breaking up a complex domain into smaller elements and finding suitable approximating functions in each element. The unknown solution φ, is approximated by a function in the equation to be solved. This interpolating function takes the values of φ at the element nodes and is used to obtain values of the unknown field at any point inside the element. Each element has its own independent interpolation function. For each element we can express the unknown field as

$$\varphi^e = \sum_{i=1}^{N_{np}} N_i \varphi_i, \tag{4.1}$$

where N_{np} is the total number of nodes in a given element and N_i is the interpolation function. In general, higher orders of the interpolation functions yields solutions closer to the actual field. As the function is required to be continuous everywhere inside the element, the solution

yields the explicit functional form, from which we can compute the value of φ at any point in the element. Further, because the field is an interpolation of values at the vertices, if two elements share vertices due to a common boundary, the field will be continuous across the boundary. Therefore, continuity of physical quantities can be translated smoothly into the FEM implementation.
The finite elements form a mesh that can be irregular and therefore computationally efficient (with finer elements where required and larger elements elsewhere). The nature of mesh elements and order of the interpolation functions can also be chosen, i. e. rectilinear elements which have straight edges and higher order functions requiring more nodal points per element. In the FEM approach, interpolating functions satisfy the governing differential equation or the variational expression in each element. It is therefore possible to solve the problem in each element separately and literally stitch together the solution. The global solution to the problem is assembled from all the elements in a global matrix equation system. The obtained solution then satisfies the requirements inside every element and is continuous across elements. Therefore it is possible to break down the requirements on an approximation function from global continuity to piecewise continuity within each element and express these in matrix form. The global matrices generated may be sparse, and the entries relating to nodes shared between elements can reduce the matrix order.

4.2 Main steps in implementation of FEM

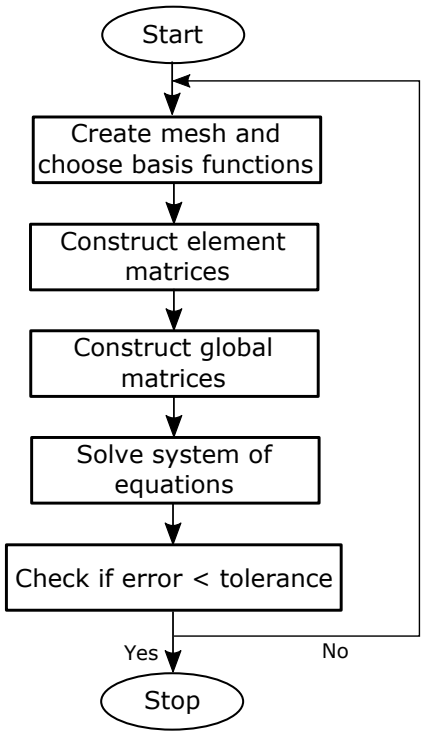

Figure 4.1: Implementation of finite element method as a flow chart.

Implementation of FEM can be illustrated as a flow chart algorithm which is convenient for such step-by-step methods (see figure 4.1). Since we are about to develop a ray tracing

algorithm for finite element discreticized volume, more detailed insight to meshing and shape functions is needed and is a topic to the next section.
More explanation for the other parts of FEM algorithm illustrated in flow chart can be found in [16] and [17] and will not be presented in this work.

4.3 Meshing domain with finite elements

As announced in previous section one of the most important step in the FEM implementation is representing the structure with smaller elements. The field values φ at the element nodes are used in the interpolation functions to approximate the unknown field as expressed in equation (4.1). By choosing different shapes and sizes of elements one can choose the number of nodes where the field is sampled. The chosen shape of elements plays a key role in determination of accuracy of structure details as well as the resolution of boundary representation.
By selecting the shape functions N_i, we are choosing the approximation of the field inside each element. Therefore, the approximation (most usually polynomial) is then fit to the values at the nodes and its coefficients determined in every element for the best fit. For example, if first-order shape functions are chosen, then a polynomial of the type $a + bx + cy$ can be used to represent the field in 2D triangular element. Coefficients to be determined are in this case a, b, c. Strong relationship is between the choice of the mesh elements and the shape function.
In a mesh, the elements do not overlap and there can not be an empty space between the elements. The elements fit together smoothly to form a connected set of small domains resembling the original structure. Resulting mesh often consists of a large number of differently sized elements. Elements that are adjacent share some nodes and may have a common boundary. A scheme needs to be developed in order to uniquely identify each node. Inside every element the nodes are numbered with $i = 1, 2, \cdots, N_{np}$ and each node has corresponding local coordinates. Each node is also assigned a global node number and has corresponding global (physical) coordinates, i.e. (x_i, y_i) for 2D Cartesian space.
There are several cathegories of most commonly used finite elements ([17]):

- Straight edges elements. These include shapes such as rectilinear ones - triangular, rectangular, quadrilateral. For higher order of discretization the edges remains straight, only the number of nodes increases as shown in figure 4.2.
- Iso-parametric elements. These elements are defined by coordinate transformation using shape functions from global coordinate system into local coordinate system. In local coordinate system geometry of these elements is unit-normalized (see figure 4.3).
- Infinite elements to simulate open or unbounded problems.

4.4 Two dimensional iso-parametric elements and shape functions

The choice of the element type is dependent on the solved problem. In this work we will use most common straight-edged elements for 2D space - first order quadrilateral and triangular

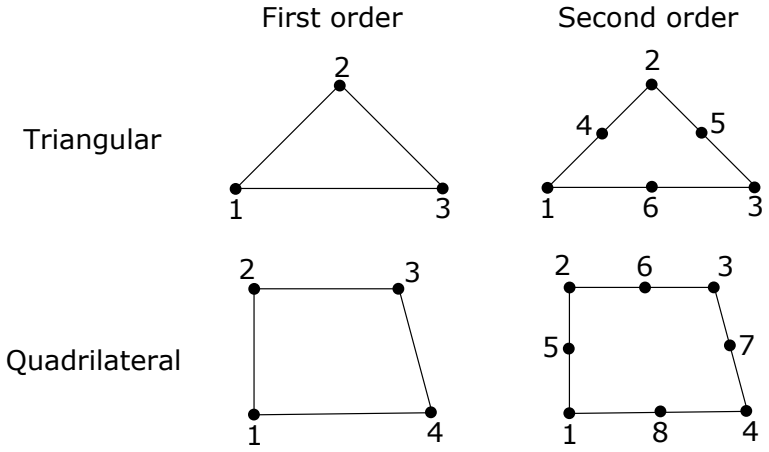

Figure 4.2: Most commonly used finite elements in 2D space.

elements. The iso-parametric version of these elements forms a fundamental part of developed ray-tracing algorithm.
Figure 4.3 shows iso-parametric first-order quadrilateral element. Local coordinates of the element ξ and η vary between -1 and 1. Local node numbering starts from lower left corner and continues in clockwise direction. Shape functions for this element with the defined node numbering scheme have the following form

$$N_1 = \frac{1}{4}(1-\xi)(1-\eta), \tag{4.2}$$

$$N_2 = \frac{1}{4}(1-\xi)(1+\eta), \tag{4.3}$$

$$N_3 = \frac{1}{4}(1+\xi)(1+\eta), \tag{4.4}$$

$$N_4 = \frac{1}{4}(1+\xi)(1-\eta). \tag{4.5}$$

Figure 4.3 also shows iso-parametric first-order triangular element. Local coordinates of the element ξ and η in this case vary between 0 and 1. Local node numbering again starts from lower left corner and continues in clockwise direction. Shape functions for this element with the defined node numbering scheme have the following form

$$N_1 = 1-\xi-\eta, \tag{4.6}$$

$$N_2 = \eta, \tag{4.7}$$

$$N_3 = \xi. \tag{4.8}$$

4.5 Deformed mesh for ray tracing of two dimensional thermally loaded optical elements

The two dimensional iso-parametric elements described in previous section play an important role in derivation of the ray-tracing algorithm procedure which will be given in following chapter. As stated earlier, the algorithm should be capable of taking into account the induced thermal deformations. Recall the previous chapter dedicated to thermo-optic effects

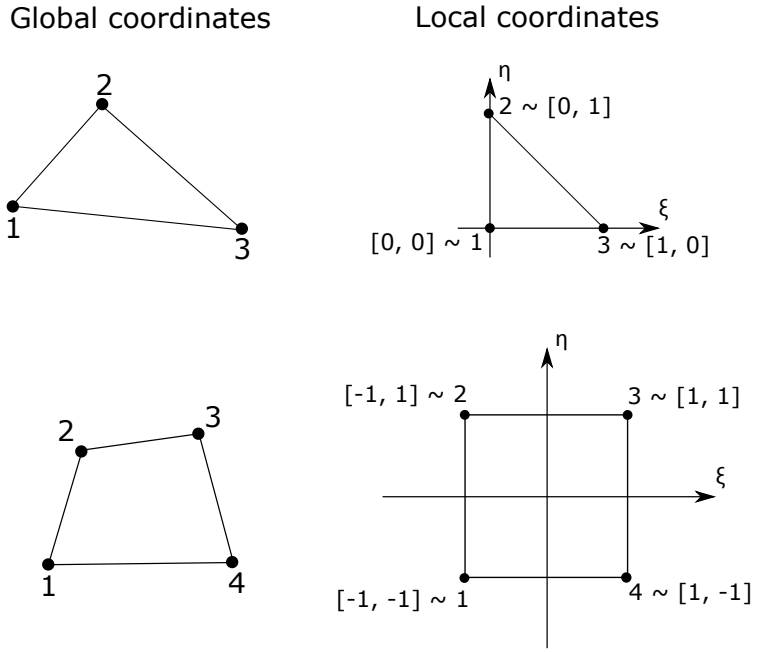

Figure 4.3: Iso-parametric elements in 2D space.

and their simplified scheme given in the figure 3.1. The deformations truly influence performance of optical systems. In this section we will describe the approach chosen to define a deformed finite element mesh.

The approach stands on translation of 2D mesh nodes (x_i, y_i) $i = 1, 2, \ldots, N$ of non-deformed mesh consisting of total N nodes. In the steady-state the nodes are shifted according to the displacement field $D(\mathbf{r}) = (u(x, y), v(x, y))$ arisen due to the thermal strain of an investigated domain resulting in a new set of nodes $(x_i + u(x_i, y_i), y_i + v_i(x_i, y_i))$, $i = 1, 2, \ldots, N$. The steady-state displacement field $D(\mathbf{r}) = (u(x, y), v(x, y))$ is obtained by solving the thermal stress model equations (3.3) to (3.5) and represents an optional input for the implemented ray-tracing algorithm. An important remark concerning thermo-mechanical analysis using FEM should be made here. The remark concerns about proper kinematical description of the deforming material under consideration. Such a choice determines the relationship between the deforming domain and the finite element mesh and strongly conditions the ability of the numerical method to deal with large distortions and provide an accurate solution. The kinematical description is associated with Lagrangian, Eulerian and possibly Arbitrary Lagrangian-Eulerian algorithms ([18]).

The Lagrangian algorithms, in which each individual node of the computational mesh follows the associated material particle during deforming, are mainly used in structural mechanics. The Lagrangian description allows an easy tracking of the free surfaces and interfaces between different materials. Its weakness is its inability to follow large distortions of the computational domain without recourse to frequent re-meshing operations.

The Eulerian algorithms are widely used in fluid dynamics. Here the computational mesh is fixed and the continuum moves with respect to the grid. In the Eulerian description, large distortions in the continuum can be handled with relative ease, but generally at the expense of precise interface definition and the resolution of flow details.

Because of the shortcomings of purely Lagrangian and Eulerian descriptions, a technique

has been developed that succeeds, to a certain extent, in combining the best features of both the Lagrangian and the Eulerian approaches. Such a technique is known as Arbitrary Eulerian-Lagrangian description abbreviated as ALE. In the ALE description, the nodes of the computational mesh may be moved with the continuum in normal Lagrangian fashion, or be held fixed as in Eulerian manner, or be moved in some arbitrarily specified way to give a continuous rezoning capability. Because of this freedom in moving the mesh offered by the ALE description, greater distortions of the continuum can be handled than would be allowed by purely Langrangian approach, and with more resolution than that afforded by a pure Eulerian approach.
Within to scope of this work we deal with the optical components most widely used in solid-state laser systems. Since the thermally induced deformations are in vast majority of such cases relatively small, the Lagrangian approach is the most suitable description here. However, in the particular example of thermo-mechanical analysis of some very thin optical components, adding the ALE codes into the set of equations solved with FEM is obligatory to achieve accurate results.

4.6 Examples of finite element meshes in COMSOL Multiphysics

Multitude of simulation programs and utilities implements finite element method for modeling and simulating physics-based problems. One of the most widely used is professional software COMSOL Multiphysics. Using COMSOL Multiphysics provides a significant amount of physics modeling functionality, including multiphysics ability. One of the target tasks of the thesis was to implement a script in MATLAB to import finite element mesh generated in COMSOL environment. Mesh designed in COMSOL is fully described with nodal coordinates and nodal connectivity array. A MATLAB script was implemented to import the useful mesh data. for purposes of ray-tracing. The script forms a structure $MESH$ which content are nodal coordinates and nodal connectivity array which both form inputs for the ray-tracing algorithm.
For illustrative purposes, a two dimensional discretized rectangle domain made of fused silica glass with dimensions of 15 x 5 cm was created in COMSOL and meshed with quadrilateral elements as shown in the figure 4.4. Figure 4.5 shows the generated mesh plotted from imported data in MATLAB environment including proper nodal (black) and element ID numbers (red). For a modified example of triangular mesh the results are depicted in figures 4.6 and 4.7.
Another example is concerned about deformed meshes. We have considered heating of the rectagular domain from the previous example with 10 W of total heat dissipated in the area. Constant temperature of 293.15 K and fixed (no deformation) constraints were assumed along both longer edges of the rectangle. The shorter edges of the rectangle were considered to be thermally isolated and free to deform. The steady-state thermo-mechanical simulation results in buckling of both rectangle shorter edges. The resulting displacement field was exported from COMSOL and contributed to the exported meshes to form a deformed mesh as described in the previous section. One of deformed shorter edges of the rectangle after zoom is depicted in the figure 4.8 for the case of quadrilateral mesh and in the figure 4.9 for the case of triangular mesh. It is worth noting how the mesh density as well as the chosen

geometrical type of finite elements influences precision of the deformed boundary representation. This fact already presented in previous sections will become crucial important in ray-tracing validation chapter.

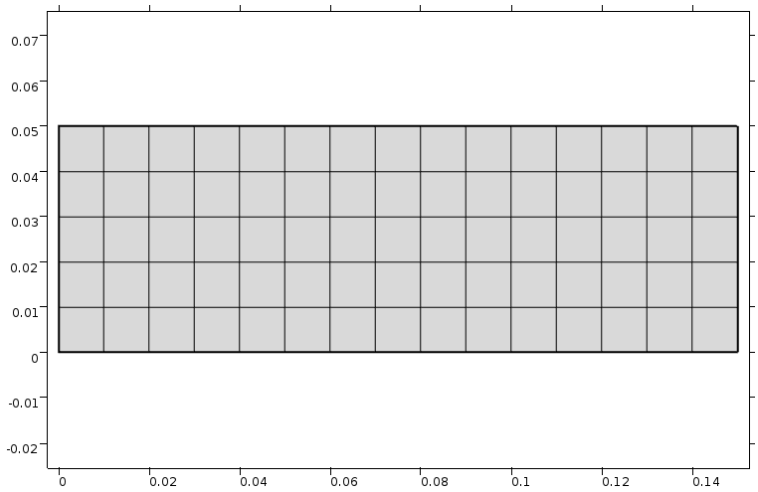

Figure 4.4: Example of quadrilateral mesh generated in COMSOL Multiphysics.

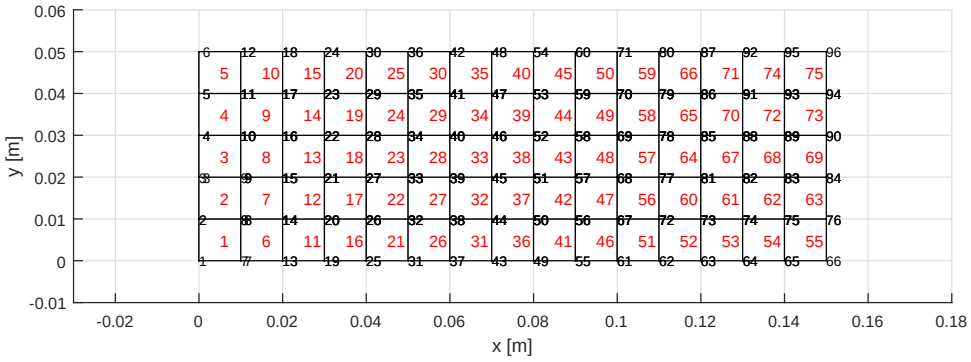

Figure 4.5: Quadrilateral mesh generated in COMSOL Multiphysics imported into MATLAB.

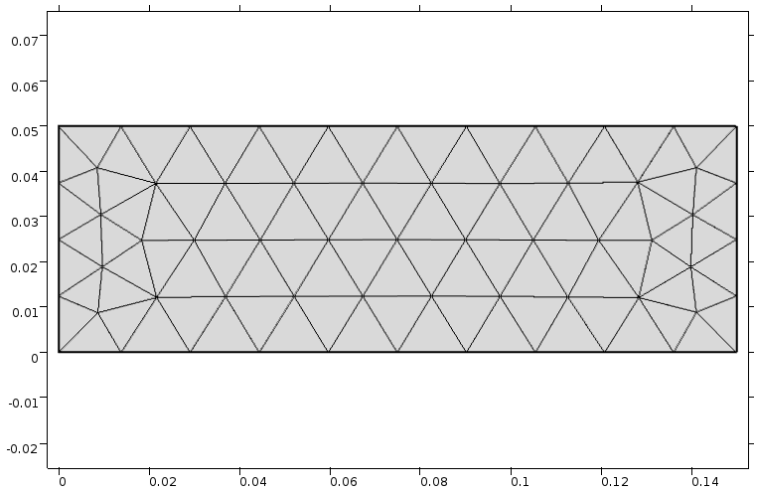

Figure 4.6: Example of triangular mesh generated in COMSOL Multiphysics.

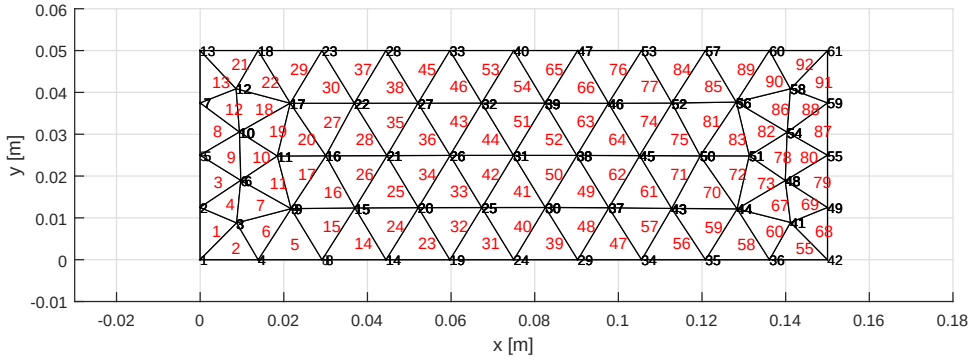

Figure 4.7: Triangular mesh generated in COMSOL Multiphysics imported into MATLAB.

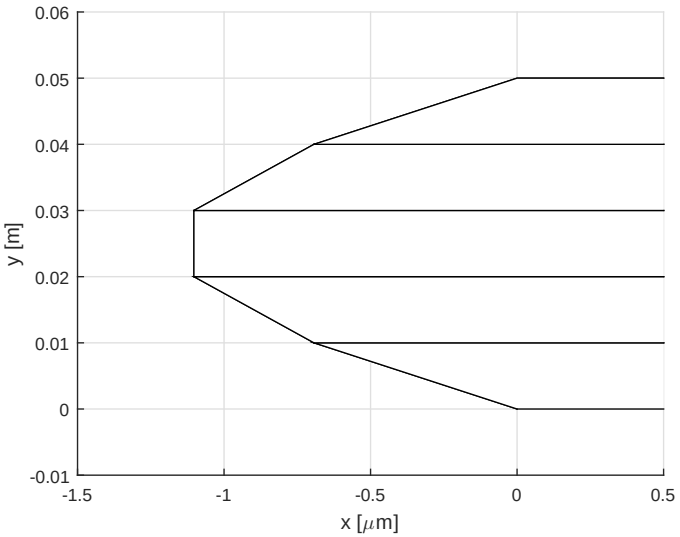

Figure 4.8: One edge of deformed quadrilateral mesh.

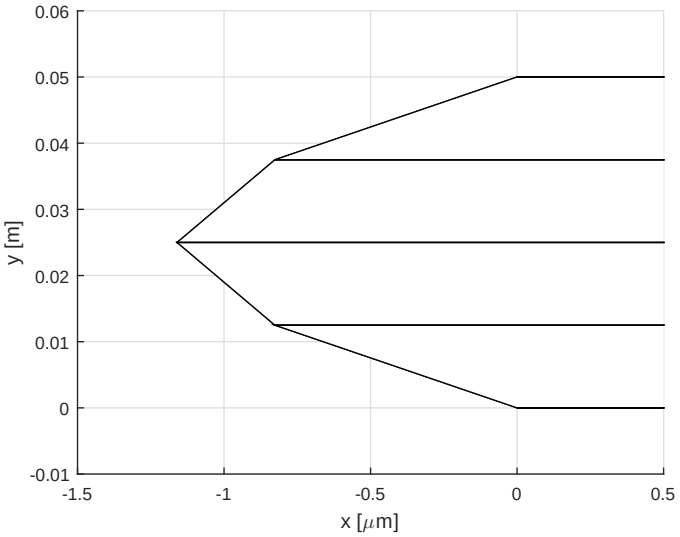

Figure 4.9: One edge of deformed triangular mesh.

Chapter 5

Ray tracing algorithm

Numerical approach presented here fully integrates the finite-element methodology to enable tracing rays directly within a discretized volume. Refractive index distribution in the volume is assumed to vary continuously between exact values at nodal positions using shape functions to interpolate values at intermediate points. Generalized gradient-index ray-trace equations are transformed into the local coordinate system of an finite element. Shape functions of the element are then used to calculate local refractive index gradient, and the resulting system of equations is cast into state-space notation suitable for numerical solving. The main relevant references referring to the chosen numerical approach are [19] - [21].

5.1 State-space ray-tracing equations in gradient-index medium

As stated before, the path of rays in a graded-index medium is obtained by solving differential ray equation (3.12)

$$\frac{d}{ds}\left[n(\mathbf{r})\frac{d\mathbf{r}}{ds}\right] = \nabla n(\mathbf{r}) \quad . \tag{5.1}$$

Recall, that $\mathbf{r}$ is the position vector of a point on the ray, $n(\mathbf{r})$ denotes the refractive index distribution in the medium and ds is a infinitesimal element of the arc length along the ray. We may introduce a change of variable $t = \int ds/n$, $dt = ds/n$ in equation (5.1) to obtain form ([19])

$$\frac{d^2\mathbf{r}}{dt^2} = n\nabla n = \frac{1}{2}\begin{bmatrix} \frac{\partial n^2}{\partial x} \\ \frac{\partial n^2}{\partial y} \end{bmatrix} \quad , \tag{5.2}$$

which dropped explicit dependence of refractive index on position. This dependency is now implied by the gradient operator. Formulation (5.2) is used to enable an abstracted concept of the ray trajectory based on Newtonian dynamics approach ([21]). One may abstract the concept of t as an independent "pseudo-time" variable and in this context the equation (5.2) represents "pseudo-acceleration" of a point $\mathbf{r}$ on the ray. This abstraction allows assembly of these "equations of motion" into a state-space system of equations, from which an elementary coordinate transformation can be derived to enable direct application within the finite-element domain. If we define a state vector for the use in 2D cartesian

space as

$$\bar{\mathbf{x}} = \left[x, y, \frac{dx}{dt}, \frac{dy}{dt} \right] \tag{5.3}$$

we may obtain full state-space representation of the differential equations of motion for a point that lies on the ray

$$\frac{d}{dt}\bar{\mathbf{x}} = \begin{bmatrix} 0_2 & I_2 \\ 0_2 & 0_2 \end{bmatrix} \bar{\mathbf{x}} + \begin{bmatrix} 0_2 \\ I_2 \end{bmatrix} \frac{1}{2} \nabla n^2 \quad , \tag{5.4}$$

where 0_2 denotes a square zero matrix 2x2 and I_2 is identity matrix of dimension 2. In equation (5.4) gradient of refractive index acts as a "force" that imparts a "pseudo-acceleration" on the ray as it propagates through a medium.
If we integrate the set of equations (5.4) with respect to t variable we obtain ray trajectory in a standard 2D cartesian space. To be able to integrate knowledge of gradient of refractive index as a function of position is required. Finite element methodology shortly introduced in previous section provides a useful framework to interpolate gradient-index within a discretized volume. This methodology is applied in following section in order to cast equation (5.4) into local element coordinate frame introducing more suitable form for ray-trace algorithm.

5.2 Ray-race equations in local coordinate frame

To cast the ray-trace equations into the local finite element coordinate frame transformation of equations (5.4) needs to be performed. Beginning with the gradient of the squared refractive index the transformation is accomplished via the Jacobian matrix J of the element as follows ([21])

$$J \nabla n^2 = J \begin{bmatrix} \frac{\partial n^2}{\partial x} \\ \frac{\partial n^2}{\partial y} \end{bmatrix} = \begin{bmatrix} \frac{\partial x}{\partial \xi} & \frac{\partial y}{\partial \xi} \\ \frac{\partial x}{\partial \eta} & \frac{\partial y}{\partial \eta} \end{bmatrix} \begin{bmatrix} \frac{\partial n^2}{\partial x} \\ \frac{\partial n^2}{\partial y} \end{bmatrix} = \begin{bmatrix} \frac{\partial n^2}{\partial \xi} \\ \frac{\partial n^2}{\partial \eta} \end{bmatrix}. \tag{5.5}$$

Derivation of Jacobian matrix is accomplished by applying finite element methodology in which we use shape functions to interpolate nodal parameters. In the case physical coordinates (x, y)

$$x(\xi, \eta) = \sum_{i=1}^{N_{np}} N_i(\xi, \eta) x_i, \tag{5.6}$$

$$y(\xi, \eta) = \sum_{i=1}^{N_{np}} N_i(\xi, \eta) y_i, \tag{5.7}$$

where N_i is the i-th shape function in node numbering scheme of the particular element, x_i and y_i are x and y coordinates of i-th element node and N_{np} is number of element nodes. It should be remainded that the number of element nodes N_{np} and the node numbering scheme depends on geometrical shape of the element as well as on the order of discretization. To proceed with Jacobian matrix form derivation it is suitable to first rewrite equations (5.6)

and (5.7) into matrix notation

$$\begin{bmatrix} x & y \end{bmatrix} = \begin{bmatrix} N_1 & N_2 & \cdots & N_{N_{np}} \end{bmatrix} \begin{bmatrix} x_1 & y_1 \\ x_2 & y_2 \\ \vdots & \vdots \\ x_{N_{np}} & y_{N_{np}} \end{bmatrix}. \tag{5.8}$$

And in this form it is obvious that the only components that have dependency on (ξ, η) are the shape functions N_i since nodal positions (x_i, y_i) are constant. The Jacobian matrix becomes

$$J = \begin{bmatrix} \frac{\partial x}{\partial \xi} & \frac{\partial y}{\partial \xi} \\ \frac{\partial x}{\partial \eta} & \frac{\partial y}{\partial \eta} \end{bmatrix} = \begin{bmatrix} \frac{\partial N_1}{\partial \xi} & \frac{\partial N_2}{\partial \xi} & \cdots & \frac{\partial N_{N_{np}}}{\partial \xi} \\ \frac{\partial N_1}{\partial \eta} & \frac{\partial N_2}{\partial \eta} & \cdots & \frac{\partial N_{N_{np}}}{\partial \eta} \end{bmatrix} \begin{bmatrix} x_1 & y_1 \\ x_2 & y_2 \\ \vdots & \vdots \\ x_{N_{np}} & y_{N_{np}} \end{bmatrix}. \tag{5.9}$$

Note that J is dependent on local coordinates, i. e. $J = J(\xi, \eta)$.
Next step is to transform the "pseudo-velocity" and "pseudo-acceleration" vector. Starting with "pseudo-velocity" vector we may use a similar approach as in Jacobian matrix derivation and obtain

$$\begin{bmatrix} \frac{dx}{dt} \\ \frac{dy}{dt} \end{bmatrix} = \begin{bmatrix} \frac{\partial x}{\partial \xi} & \frac{\partial x}{\partial \eta} \\ \frac{\partial y}{\partial \xi} & \frac{\partial y}{\partial \eta} \end{bmatrix} \begin{bmatrix} \frac{d\xi}{dt} \\ \frac{d\eta}{dt} \end{bmatrix} = J^T \begin{bmatrix} \frac{d\xi}{dt} \\ \frac{d\eta}{dt} \end{bmatrix}. \tag{5.10}$$

"Pseudo-acceleration" vector is then obtained by differentiation of (5.10) with respect to t variable.

$$\begin{bmatrix} \frac{d^2x}{dt^2} \\ \frac{d^2y}{dt^2} \end{bmatrix} = \frac{d}{dt} \begin{bmatrix} \frac{dx}{dt} \\ \frac{dy}{dt} \end{bmatrix} = \frac{d}{dt} \left\{ J^T \begin{bmatrix} \frac{d\xi}{dt} \\ \frac{d\eta}{dt} \end{bmatrix} \right\} = \frac{dJ^T}{dt} \begin{bmatrix} \frac{d\xi}{dt} \\ \frac{d\eta}{dt} \end{bmatrix} + J^T \begin{bmatrix} \frac{d^2\xi}{dt^2} \\ \frac{d^2\eta}{dt^2} \end{bmatrix}. \tag{5.11}$$

After substitution of expressions (5.5), (5.10) and (5.11) into equation (5.4) and rearrangement we obtain equation in terms of local coordinate frame as follows

$$\begin{bmatrix} \frac{d^2\xi}{dt^2} \\ \frac{d^2\eta}{dt^2} \end{bmatrix} = J^{-T} \left\{ \frac{1}{2} J^{-1} \begin{bmatrix} \frac{\partial n^2}{\partial \xi} \\ \frac{\partial n^2}{\partial \eta} \end{bmatrix} - \frac{dJ^T}{dt} \begin{bmatrix} \frac{d\xi}{dt} \\ \frac{d\eta}{dt} \end{bmatrix} \right\}, \tag{5.12}$$

where J^{-T} stands for transposed inverse of Jacobian matrix. Apart from the Jacobian matrix J equation (5.12) also requires the derivative with respect to t variable dJ/dt. This is accomplished by extending the approach in equation (5.9), namely

$$\frac{dJ}{dt} = \frac{d}{dt} \begin{bmatrix} \frac{\partial N_1}{\partial \xi} & \frac{\partial N_2}{\partial \xi} & \cdots & \frac{\partial N_{N_{np}}}{\partial \xi} \\ \frac{\partial N_1}{\partial \eta} & \frac{\partial N_2}{\partial \eta} & \cdots & \frac{\partial N_{N_{np}}}{\partial \eta} \end{bmatrix} \begin{bmatrix} x_1 & y_1 \\ x_2 & y_2 \\ \vdots & \vdots \\ x_{N_{np}} & y_{N_{np}} \end{bmatrix}, \tag{5.13}$$

where nodal positions are constant, so the time derivative applies only to the matrix of shape function derivatives. After applying the chain rule and rearrangement we obtain following

form of Jacobian matrix time derivative

$$\frac{dJ}{dt} = \left\{ \begin{array}{l} \begin{bmatrix} \frac{d\xi}{dt} \\ \frac{d\eta}{dt} \end{bmatrix}^T \begin{bmatrix} \frac{\partial^2 N_1}{\partial \xi^2} & \frac{\partial^2 N_2}{\partial \xi^2} & \cdots & \frac{\partial^2 N_{N_{np}}}{\partial \xi^2} \\ \frac{\partial^2 N_1}{\partial \xi \partial \eta} & \frac{\partial^2 N_2}{\partial \xi \partial \eta} & \cdots & \frac{\partial^2 N_{N_{np}}}{\partial \xi \partial \eta} \end{bmatrix} \\ \begin{bmatrix} \frac{d\xi}{dt} \\ \frac{d\eta}{dt} \end{bmatrix}^T \begin{bmatrix} \frac{\partial^2 N_1}{\partial \eta \partial \xi} & \frac{\partial^2 N_2}{\partial \eta \partial \xi} & \cdots & \frac{\partial^2 N_{N_{np}}}{\partial \eta \partial \xi} \\ \frac{\partial^2 N_1}{\partial \eta^2} & \frac{\partial^2 N_2}{\partial \eta^2} & \cdots & \frac{\partial^2 N_{N_{np}}}{\partial \eta^2} \end{bmatrix} \end{array} \right\} \begin{bmatrix} x_1 & y_1 \\ x_2 & y_2 \\ \vdots & \vdots \\ x_{N_{np}} & y_{N_{np}} \end{bmatrix}. \tag{5.14}$$

It is worth noting that for finite element with first-order shape functions, the second derivatives are zero and therefore dJ/dt is also zero.
The last part in equation (5.12) that needs to be evaluated is gradient of squared refractive index. Applying the similar procedure as before we get

$$\begin{bmatrix} \frac{\partial n^2}{\partial \xi} \\ \frac{\partial n^2}{\partial \eta} \end{bmatrix} = \begin{bmatrix} \frac{\partial N_1}{\partial \xi} & \frac{\partial N_2}{\partial \xi} & \cdots & \frac{\partial N_{N_{np}}}{\partial \xi} \\ \frac{\partial N_1}{\partial \eta} & \frac{\partial N_2}{\partial \eta} & \cdots & \frac{\partial N_{N_{np}}}{\partial \eta} \end{bmatrix} \begin{bmatrix} n_1^2 \\ n_2^2 \\ \vdots \\ n_{N_{np}}^2 \end{bmatrix}. \tag{5.15}$$

This can be applied to any parameter p with values defined in nodal points such as temperature, displacements, etc.
Let us summarise what has been done so far. We have introduced differential ray equation (5.2) and applied finite element methodology to use this equation in discretized volume. In this manner we have obtained equation (5.12). Let us put equations (5.2) and (5.12) for a moment next to each other to realise some important aspects of this approach.

$$\begin{bmatrix} \frac{d^2x}{dt^2} \\ \frac{d^2y}{dt^2} \end{bmatrix} = \frac{1}{2} \begin{bmatrix} \frac{\partial n^2}{\partial x} \\ \frac{\partial n^2}{\partial y} \end{bmatrix} \tag{5.16}$$

$$\begin{bmatrix} \frac{d^2\xi}{dt^2} \\ \frac{d^2\eta}{dt^2} \end{bmatrix} = J^{-T} \left\{ \frac{1}{2} J^{-1} \begin{bmatrix} \frac{\partial n^2}{\partial \xi} \\ \frac{\partial n^2}{\partial \eta} \end{bmatrix} - \frac{dJ^T}{dt} \begin{bmatrix} \frac{d\xi}{dt} \\ \frac{d\eta}{dt} \end{bmatrix} \right\}. \tag{5.17}$$

Equation (5.17) is the analog of equation (5.16) cast in the (ξ, η) domain. However, if we compare them, it is obvious that on right side of equation (5.16) there is only one term, whereas in equation (5.17) there are two. The left-most bracketed term in equation (5.17) is proportional to the gradient of n^2 in the (ξ, η) domain. This term is obvious analog of the term on the right side of equation (5.16) in the physical domain. However, the right-most bracketed component in equation (5.17) seems to have no apparent analog in physical domain.
This additive term depending on both velocity and the rate of change of the Jacobian, can be understood by considering mapping the ray trajectory from physical into local coordinate space ([21]). For a homogeneous medium the gradient of n^2 in the physical domain is equal to zero and the ray trajectory within this medium remains linear. However, if we consider mapping of some skew aspect of the element (i. e. mesh deformations as a consequence of thermal stress) from physical domain into local domain the space within the element becomes in general curvilinear. In other word linear ray trajectory in physical domain is generally curved in local coordinate system. And this particular aspect of mapping is represented in equation (5.17) by the second term dependent on velocity and the rate of change of the Jacobian.

5.3 Transition between two elements within the volume

For the purposes of tracing rays through a finite element domain we have derived equation (5.12) which integrated with respect to t variable through the volume provides solution for the ray trajectory. However, procedure to deal with transition between the local coordinate frames of intersected elements still needs to be established. One may consider transformation from terminal element local frame into physical domain frame and then transformation into the local coordinate frame of the entrance element. This approach is correct but it is beneficial to obtain one step transformation to reduce computational demands and accumulation of numerical errors. One step transformation was developed for the transition between two element of the same type, i. e. transition between two quadrilateral elements or between two triangular elements. For a transition between two different types of finite elements no computationally effective method was developed so far and therefore it stands on general transformation from terminal element local frame into physical domain frame and then transformation into the local coordinate frame of the entrance element.

5.3.1 Transition between two quadrilateral elements

First discussed will be the case of transition between two quadrilateral elements. In the plane of transition which is shared by two elements, the ray coordinates maintain the same absolute values in both local coordinate systems. Coordinates are transformed by relative rotation of the axes

$$\begin{bmatrix} \xi_2 \\ \eta_2 \end{bmatrix} = T \begin{bmatrix} \xi_1 \\ \eta_1 \end{bmatrix}, \tag{5.18}$$

where T is the transformation matrix. To obtain the transformation matrix we first collect local coordinates of the nodes contained in common transition face. Basis is then formed from vectors derived from these local coordinates as follows

$$v_{1a} = \text{mean} \begin{pmatrix} \xi \\ \eta \end{pmatrix}_{EL1}, \tag{5.19}$$

$$v_{2a} = \text{mean} \begin{pmatrix} \xi \\ \eta \end{pmatrix}_{EL2}. \tag{5.20}$$

The remaining vectors v_{1b} and v_{2b} to form the basis are orthogonal to derived ones as shown on an illustrative example on figure 5.1. The transformation matrix is then

$$T = \begin{bmatrix} v_{1a} & v_{1b} \end{bmatrix} \begin{bmatrix} v_{2a} & v_{2b} \end{bmatrix}^{-1}. \tag{5.21}$$

Apart from the ray coordinates we need to transform the ray directions. Using equation (5.10) we deduce that

$$\begin{bmatrix} \frac{dx}{dt} \\ \frac{dy}{dt} \end{bmatrix} = J_1^T \begin{bmatrix} \frac{d\xi_1}{dt} \\ \frac{d\eta_1}{dt} \end{bmatrix} = J_2^T \begin{bmatrix} \frac{d\xi_2}{dt} \\ \frac{d\eta_2}{dt} \end{bmatrix}, \tag{5.22}$$

from which after rearrangement yields

$$\begin{bmatrix} \frac{d\xi_2}{dt} \\ \frac{d\eta_2}{dt} \end{bmatrix} = J_2^{-T} J_1^T \begin{bmatrix} \frac{d\xi_1}{dt} \\ \frac{d\eta_1}{dt} \end{bmatrix}. \tag{5.23}$$

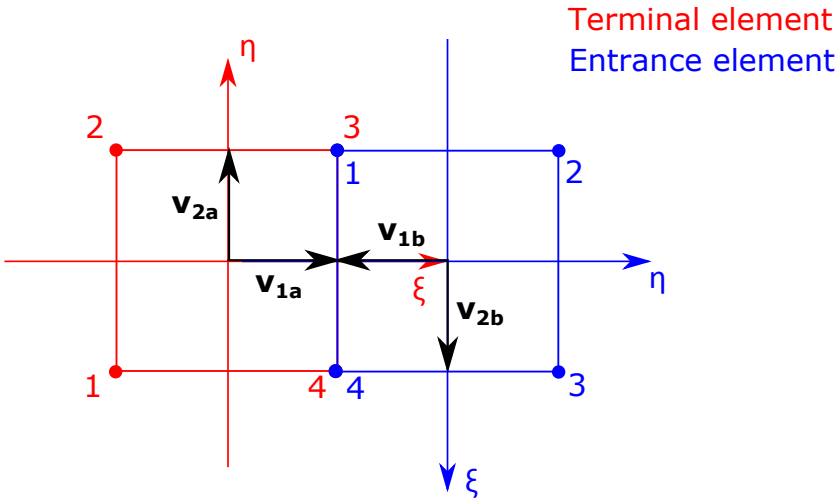

Figure 5.1: Examples of possible transition between two iso-parametric quadrilateral elements.

5.3.2 Transition between two triangular elements

The second procedure presented will be for the case of transition between two triangular elements. Transformation of the ray directions remains the same as in the case of transition between quadrilateral elements. Using equation (5.23) we may obtain the ray directions with respect to the entrance element. To transform terminal point coordinates into local coordinate frame of the entrance element there is no need of forming transformation matrix as in the previous case. We may consider the fact that there are only several possibilities for two triangles sharing common edge. Figure 5.2 shows two out of these nine possible configurations. The most left scheme depicts transition of ray from edge number (3) in the terminal element into edge number (1) in the entrance element, whereas the most right scheme depicts transition of ray from edge number (2) in the terminal element into the edge with the same number in the entrance element. If we proceed through all configurations, we may obtain 9 simple formulas for the coordinate transformation between two local coordinate frames of triangular elements,

$$(1) \rightarrow (1) \quad [\xi,\eta] \rightarrow [0, 1-\eta] \tag{5.24}$$
$$(1) \rightarrow (2) \quad [\xi,\eta] \rightarrow [1-\eta, \eta] \tag{5.25}$$
$$(1) \rightarrow (3) \quad [\xi,\eta] \rightarrow [\eta, 0] \tag{5.26}$$
$$(2) \rightarrow (1) \quad [\xi,\eta] \rightarrow [0, \eta] \tag{5.27}$$
$$(2) \rightarrow (2) \quad [\xi,\eta] \rightarrow [\eta, \xi] \tag{5.28}$$
$$(2) \rightarrow (3) \quad [\xi,\eta] \rightarrow [\xi, 0] \tag{5.29}$$
$$(3) \rightarrow (1) \quad [\xi,\eta] \rightarrow [0, \xi] \tag{5.30}$$
$$(3) \rightarrow (2) \quad [\xi,\eta] \rightarrow [\xi, 1-\xi] \tag{5.31}$$
$$(3) \rightarrow (3) \quad [\xi,\eta] \rightarrow [1-\xi, 0] \tag{5.32}$$

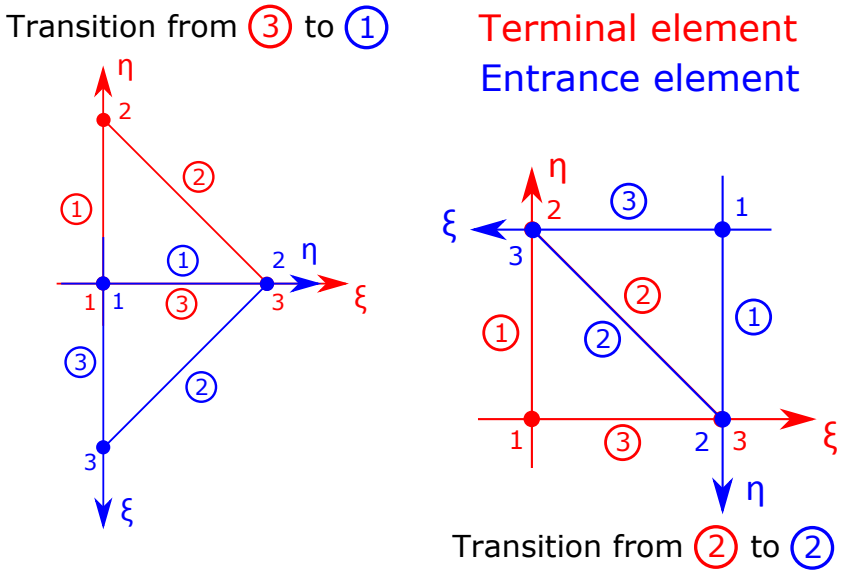

Figure 5.2: Examples of possible configurations for transition between two triangular elements.

5.4 Physical coordinates to local coordinate frame transformation

As presented before, finite-element methodology provides a direct method to interpolate physical coordinates within a certain finite element using shape functions and local coordinates (equations (5.6) and (5.7)). This conversion is typically nonlinear in nature and inverting the transformation to find local coordinates for a given set of physical coordinates can be ill posed and introduce errors into the derived local coordinates.
Therefore more robust method based on gradient-descent approach was implemented in order to increase ray tracing algorithm reliability. We define a cost function as error squared between original physical coordinates (x, y) subjected to transformation and their interpolation using shape functions, namely

$$c(x, y, \xi, \eta) = |err|^2 = err^T * err, \tag{5.33}$$

where

$$err = \begin{bmatrix} x \\ y \end{bmatrix} - \begin{bmatrix} x_1 & x_2 & \cdots & x_{N_{np}} \\ y_1 & y_2 & \cdots & y_{N_{np}} \end{bmatrix} \begin{bmatrix} N_1(\xi, \eta) \\ N_2(\xi, \eta) \\ \vdots \\ N_{N_{np}}(\xi, \eta) \end{bmatrix}. \tag{5.34}$$

The gradient of the cost function c is derived as follows

$$\nabla c(x, y, \xi, \eta) = 2(\nabla err) * err = -2J * err. \tag{5.35}$$

Formulas (5.33) and (5.35) can be subjected to any gradient-descent algorithm. We have used conjugate-gradient minimization algorithm ([22]).

5.5 Ray tracing algorithm

So far we have introduced mathematical basis for tracing rays in gradient-index medium, we have integrated finite element methodology to apply introduced mathematical phenomena on discretized finite element volume and finally we have established procedure for ray transition between two finite elements within the volume. Previous sections form a basis for ray tracing algorithm which will be described now in detail.
Before launching the algorithm a basic set of assumptions about algorithm inputs must be fulfilled.

- The incoming ray definition is available in the form of a vector $[x_r, y_r, \alpha_r]^T$, where
  - x_r, y_r are coordinates of the starting point of the ray in physical coordinate frame
  - α_r is the angle between the ray and the positive half axis x in physical coordinate frame.
- Full set of finite-element mesh nodes of the investigated discrete volume is available with corresponding properties such as
  - ID number of a node ,
  - position of a node in physical coordinate frame ,
  - value of n^2 in a node,
  - any other parameter values relevant for ray-tracing, i. e. displacement of a node if we consider deformations of the medium etc.
- Full set of finite-element volume vertices with corresponding nodal ID numbers is available.
- Full set of finite-element volume edges is available.
- Full set of finite-element mesh elements is available with corresponding properties such as
  - ID number of an element ,
  - the node ID numbers of nodes related to the element .
- Global numerical tolerance value is set to reduce accumulating of numerical errors.

Once all the assumptions are fulfilled the ray trace algorithm may start and proceed in following step-by-step manner. The algorithm is quite complex, hence its flow chart is depicted in figure 5.4 for the sake of lucidity.

1. Localization of the finite-element which the incoming ray strikes first.
   (a) Estimate the ray incidence point by calculating intersection between the ray and the finite volume. Since this algorithm is restricted into two dimensional space the finite volume is generally a polygon. Full set of finite-element volume vertices is one of the inputs to the algorithm, hence the estimated ray incidence point (x_{RO}, y_{RO}) is a result of ray-polygon intersection problem which is widely utilized in the field of ray tracing.

(b) The next step is to find k nearest nodes[1] to (x_{RO}, y_{RO}) from the set of finite-element volume edges. A brute-force search was implemented in this case although some more advanced algorithms are certainly available and could provide more efficient solution to this problem. Once the k nearest nodes are discovered, set of elements is searched to find the finite element containing discovered nodes. However, this "element-candidate" might not be the correct one as depicted in figure 5.3 and therefore we need to check by subjecting the "element-candidate" again to ray-polygon intersection calculation. If we obtain a solution for intersection (x_{RE}, y_{RE}) which is not located on the edge of finite-volume or the ray simply does not strike the "element-candidate" we have to search for the correct incident element among the elements neighboring to the "element-candidate".

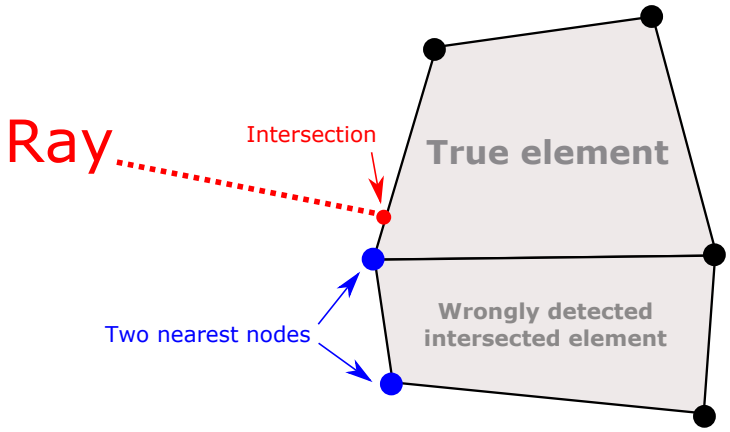

Figure 5.3: Example of wrongly detected intersection element.

2. Once the correct intersection point (x_{RE}, y_{RE}) is known we transform its physical coordinates into local coordinate coordinates (ξ_0, η_0) of the intersected element using approach presented in section 5.4.

3. Determine ray refraction at the incident point and prepare initial values for numerical integration.

   (a) Interpolate the refractive index n_0 of the incident element at the point of intersection using expression (5.15).

   (b) Calculate surface normal at the point of incidence.

   (c) Determine ray direction α_0 of refracted ray using calculated surface normal, ambient index of refraction n_a, interpolated refractive index and initial ray direction α_r .

   (d) Determine initial ray "pseudo-velocity" in local coordinate frame of the intersected element using equation (5.10)

$$\left[\begin{array}{c} \frac{d\xi}{dt} \\ \frac{d\eta}{dt} \end{array}\right]_{\xi_0,\eta_0} = J^{-T} \left[\begin{array}{c} \frac{dx}{dt} \\ \frac{dy}{dt} \end{array}\right]_{x_{RE},y_{RE}} = J^{-T} n \left[\begin{array}{c} \cos(\alpha_0) \\ \sin(\alpha_0) \end{array}\right]. \tag{5.36}$$

[1]The parameter k was set to equal to 2 in order to detect the first-intersected edge.

4. Integrate the ray trajectory through the intersected element using equation (5.12) until it intersects one of element edges (value of ξ or η is equal to ± 1).

5. Is the terminal edge on the edge of the finite volume ?

   (a) If it is not, search for a neighbour finite element to which the terminal edge belongs. Perform the transition between the old element and the new one and then proceed with numerical integration according to the step 4.

   (b) If it is, first use the element shape functions to interpolate refractive index n_e at the terminal point (ξ_e, η_e), then calculate the exiting ray direction as follows

$$\begin{bmatrix} \cos(\alpha_0) \\ \sin(\alpha_0) \end{bmatrix} = \frac{1}{n_e} J^T \begin{bmatrix} \frac{d\xi}{dt} \\ \frac{d\eta}{dt} \end{bmatrix}_{\xi_e, \eta_e} \tag{5.37}$$

   and finally determine the ray refraction of the exiting ray as in the step 3c.

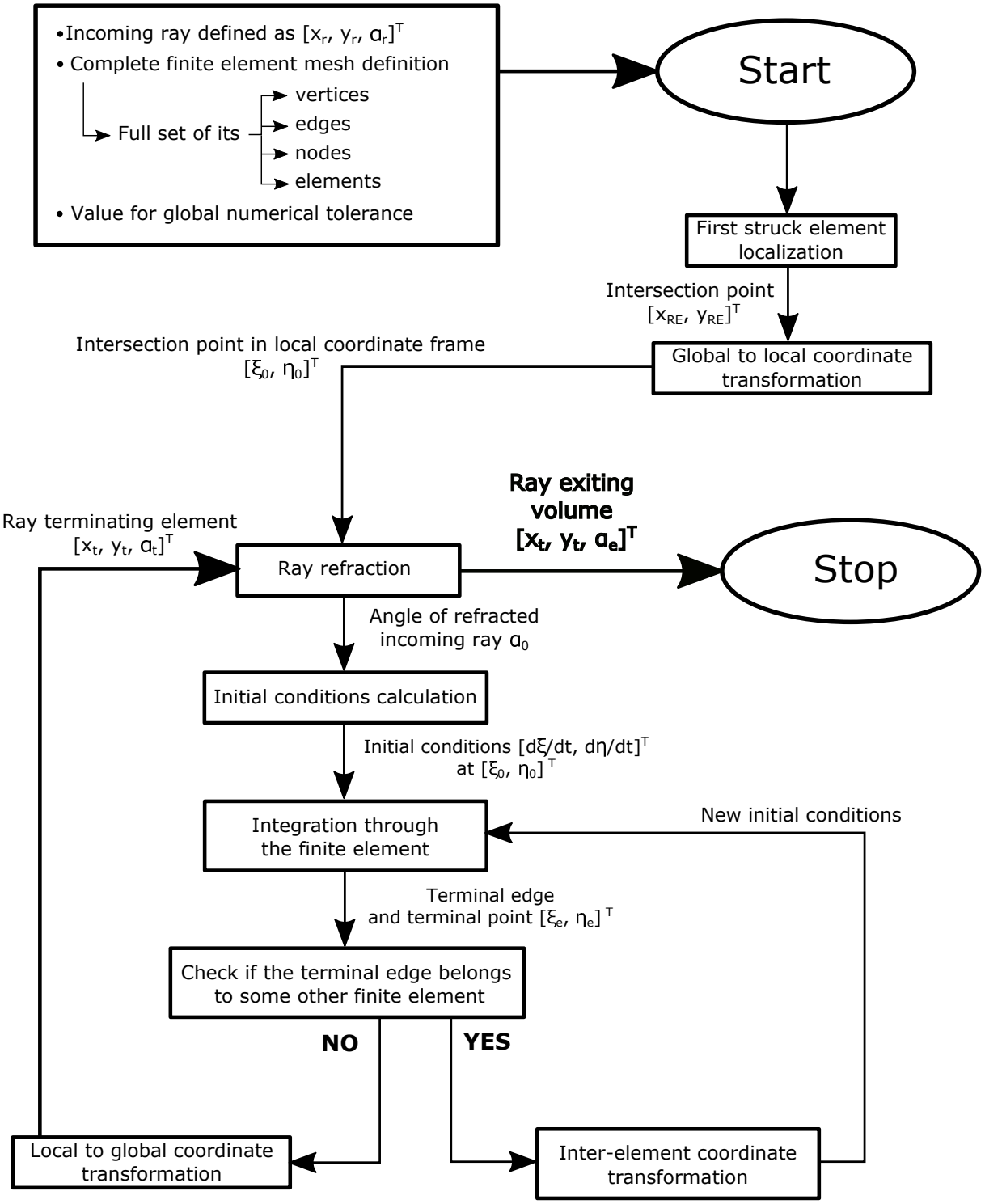

Figure 5.4: Ray tracing algorithm as a flow chart.

Chapter 6

Validation of the implemented ray tracing algorithm

Ray tracing algorithm described in the previous chapter was implemented in MATLAB environment. This section is dedicated to a several numerical simulations which demonstrates validity of the implemented algorithm. Performance verification proceeds in step-by-step manner from simulations investigating rays propagation in homogeneous refractive index media to ray propagation in graded-index field.

6.1 Homogeneous refractive index media

6.1.1 Rectangular glass domain with normal and skew incidence rays

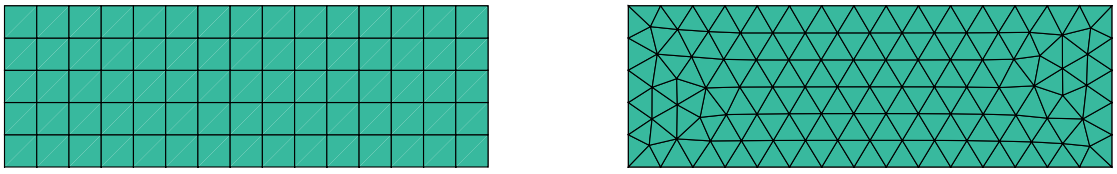

(a) Quadrilateral mesh.

(b) Triangular mesh.

Figure 6.1: Two dimensional discretized rectangle fused silica glass domain with dimensions of 15 x 5 cm.

Two dimensional discretized rectangular fused silica glass domain with dimensions of 15

x 5 *cm* used in section 4.6 will be used in the first set of demonstrative simulations. The domain was meshed with a) 75 (15 x 5) quadrilateral elements and with b) 188 triangular elements in order to test the algorithm behavior for both considered types of mesh (see figure 6.1a and 6.1b).
The first presented simulation will be the case of tracing 10 rays with normal incidence to one of the edges of the domain. The obtained ray trajectories are shown on figures 6.2a and 6.2b for the case of quadrilateral mesh and on figures 6.3a and 6.3b for the triangular mesh respectfully. As expected rays propagate linearly through the medium and then terminates it without any change in direction.

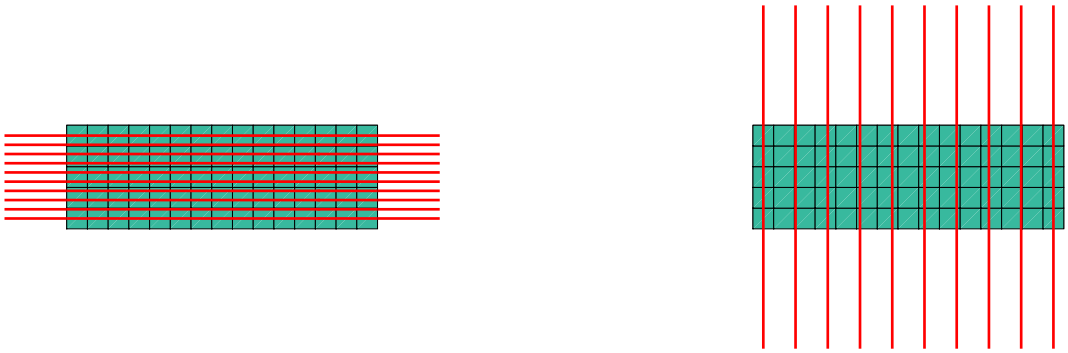

(a) Propagation from the left edge to the right.

(b) Propagation from the bottom edge to the top.

Figure 6.2: Results for tracing rays with normal incidence to one of the edges of the domain, quadrilateral mesh.

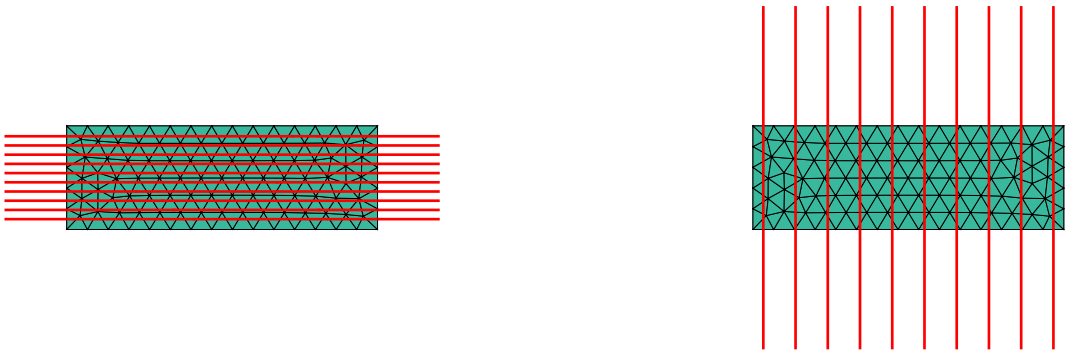

(a) Propagation from the left edge to the right.

(b) Propagation from the bottom edge to the top.

Figure 6.3: Results for tracing rays with normal incidence to one of the edges of the domain, triangular mesh.

The second numerical simulation is a slight modification of the previous one. Now we will consider skew incidence and simulate travelling of several rays with 10 and 45 degree angle of incidence to one of the edges of the domain. Indeed, the direction angle of out-coming rays

should remain the same after propagating through a constant refractive index domain. The resulting ray trajectories are shown on figures 6.4a and 6.4b for the case of quadrilateral mesh and on figures 6.5a and 6.5b for the triangular mesh. The calculated RMS error between

(a) 10 degree incidence.

(b) 45 degree incidence.

Figure 6.4: Results for tracing skew rays incident with one of the edges of the domain, quadrilateral mesh.

(a) 10 degree incidence.

(b) 45 degree incidence.

Figure 6.5: Results for tracing skew rays incident with one of the edges of the domain, triangular mesh.

the input and output ray direction angles of simulated ray trajectories had for both mesh types and for both considered incident angles order of 10^{-16} which is of the same order as the floating-point relative accuracy on simulating computer station.

6.1.2 Thin lens spherical abberation

Although the above mentioned simulations suggest a proper functionality of the algorithm for homogeneous refractive index media, more detailed investigation of valid refraction on domain boundaries was done on an example of thin lens with spherical abberation.

Spherical abberation is an optical effect which cause that monochromatic rays from a point source do not converge to a single image point image after being refracted by a lens. Rays that strike the lens near to its edge are focused closer in comparision with those that strike nearer the centre (paraxial rays) ([3]).
For a thin lens of very small aperture, and for objects very near the axis of the lens, the relation between the object distance u and image distance v may be expressed as ([23])

$$\frac{1}{u} + \frac{1}{v} = \frac{1}{f_0} \quad , \tag{6.1}$$

where f_0 is the paraxial focal length of the lens, which is given by following equation ([23], [24])

$$\frac{1}{f_0} = (n-1)\left[\frac{1}{R_1} - \frac{1}{R_2} + \frac{(n-1)d}{nR_1R_2}\right] \quad , \tag{6.2}$$

where R_1 and R_2 denotes radii of curvature of spherical surfaces of the lens, n is refractive index and d stands the distance along the lens axis between the two surface vertices (the lens thickness). For a thin lens approximation $d << R_1$ or $d << R_2$ has to be guaranteed.
The difference Δf between the focal length for paraxial rays f_0 and rays being incident with the lens at distance h from the optical axis is approximately given by

$$\Delta f = f_0 - f(h) \approx \frac{1}{2}Kh^2 \quad . \tag{6.3}$$

The parameter K is a characteristic measure of the spherical aberration of the focusing element. For a thin spherical lens it can be written ([23], [24])

$$K = \frac{1}{4f_0n(n-1)}\left[\frac{n+2}{n-1}q^2 + 4(n+1)qp + (3n+2)(n-1)p^2 + \frac{n^3}{n-1}\right] \quad , \tag{6.4}$$

where $q = (1-R_1/R_2)/(1+R_1/R_2)$ is called the shape factor and $p = 2f/u - 1 = 1 - 2f/v = (1-u/v)/(1+u/v)$ denotes the position factor.
For the particular values of $R_1 = R_2 = 0.25$ m, $d = 1$ cm, $n = 1.45$ a fused silica glass domain was created in COMSOL environment, meshed with 1762 triangular elements and imported to MATLAB. We have considered $p = -1$ corresponding to a object placed in $u = \infty$ imaged in distance $v = f_0$. The ray tracing results from the MATLAB algorithm are depicted in the figure 6.6a[1]. Rays with the same colour are incident with the lens in the same distance h from the optical axis. The spherical abberations are more obvious if we zoom a little bit the focal point area (see figure 6.6b) to clearly see that rays that strike the lens near to its edge are focused closer (red rays) in comparison with those that strike nearer the centre (violet rays). We may plot the focal point $f(h)$ as a function of h using equations (6.3) and (6.4) and compare with numerical results. The graph showing the comparison as well as the relative error between analytical and numerical solution is depicted in the figure 6.7. The relative error is growing up to 1.4% for this particular configuration. The main cause consist in limitations of analytical model which holds only for an infinitely thin lens. Hence, even though the ratio $d/R = 0.04$ is significantly less than 1 and therefore the assumption of thin lens approximation is relevantly reasonable, the error is relatively high.

[1]The lens appears to be non-transparent because the plot also contains high-density mesh.

Let us consider different configuration with lower d/R ratio and observe if the relative error would be less than in the previous case. For the values of $R_1 = R_2 = 1.25$m and $d = 0.5$mm we get approximately ten times less ratio $d/R = 0.004$ and if we plot and compare analytical and numerical results[2] for the focal point $f(h)$ we may observe, that the relative error is in this new configuration much lower (approximately 60 times lower) than in the previous one (see figure 6.8). Based on this observation we may conclude that as $d/R \to 0$ the numerical solution approaches to the analytical solution.

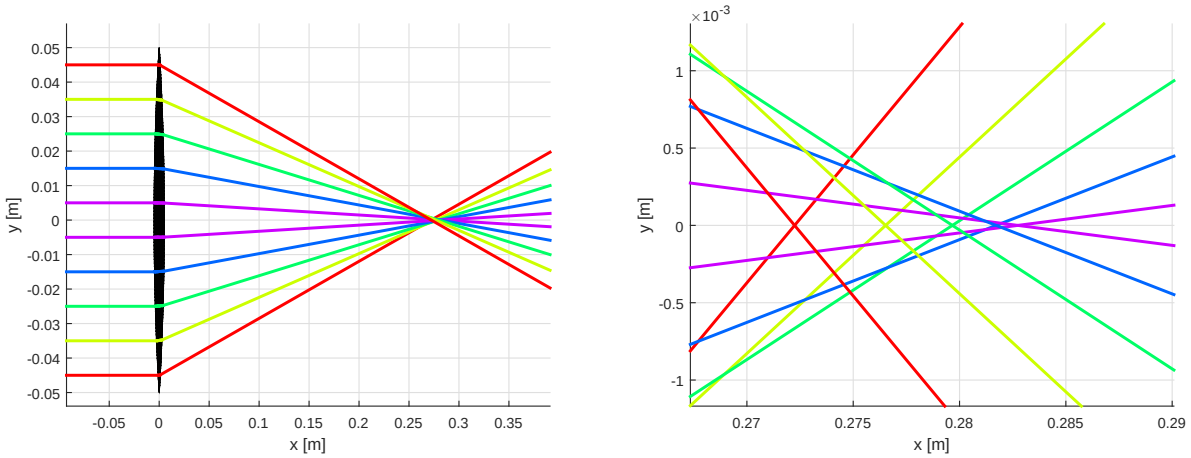

(a) (b)

Figure 6.6: Results for tracing rays through a thin lens.

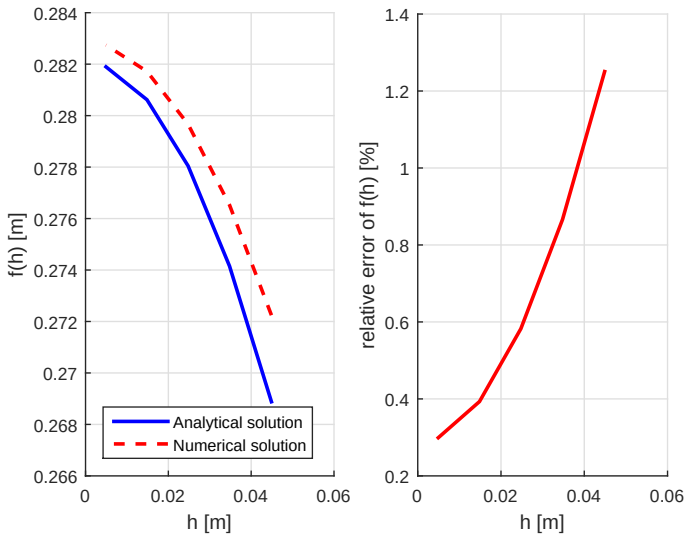

Figure 6.7: Focal point simulation results compared to analytical model, $d/R = 0.04$.

[2]The computational mesh was generated with the same parameters as in the previous case.

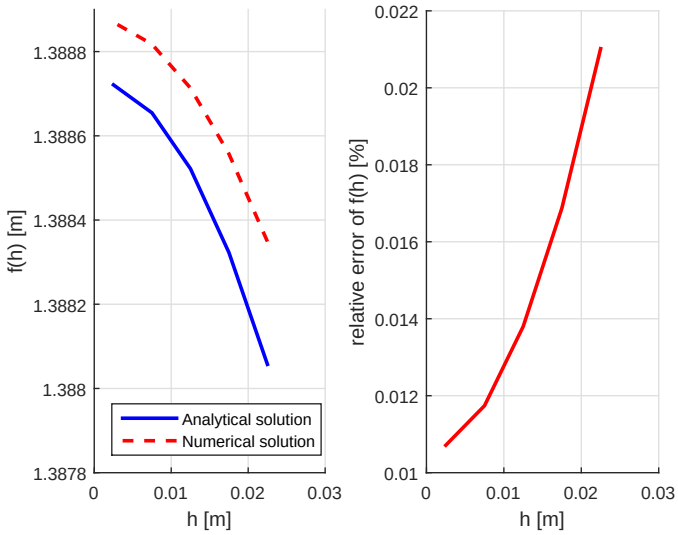

Figure 6.8: Focal point simulation results compared to analytical model, $d/R = 0.004$.

6.2 Inhomogeneous refractive index media

On the example of rectangular glass domain incident with set of normal and skew rays and on the example of thin lens we have so far verified the implemented algorithm for simulations of ray propagation in homogeneous refractive index media. The next step is to validate the performance for inhomogeneous refractive index media which is more general case. As in the thin lens example we will use comparison approach which stands on comparing a closed-form solution with the numerical results. To obtain the analytical formula for the ray trajectory in particular graded index medium, one has to solve the differential ray equation (3.12). The task is generally not trivial and therefore it is convenient to consider simplifications. The inhomogeneity of the refractive index will be assumed only as a result of non-uniform temperature distribution. Effect of thermal deformations will be neglected for the sake of simplicity.

Another simplification outcomes from considering a cylindrical geometry which is widely used within the solid-state laser systems for both active media and other optical elements. When investigating thermo-optical effects in the medium with cylindrical geometry one can in certain cases take advantage of geometrical symmetry and treat the medium as a two dimensional axial-symmetric domain. In our examined case we will consider axial-symmetric glass rod for which hold that the height (or length) of the cylinder is greater than its diameter. Second widely used cylindrical geometry used in solid-state laser systems is an axial-symmetric disc (cylinder diameter is greater than its height). Because of the geometric analogy between the disc and the rod geometry the derived solutions for a rod holds also for a disc[3]. Based on this fact model equations for axial-symmetric cylindrical geometry are presented first and then only the rod geometry is examined for particular parameters.

[3]For the same set of assumptions and considered simplifications during the solution derivation.

6.2.1 Axially symmetric cylindrical geometry

The heat generated within a cylinder by a pump-light absorption is considered to be removed by a coolant flowing along the cylindrical surface. With the assumption of uniform internal heat generation and thermal isolation of top and bottom faces of the rod, we may neglect the small variation of coolant temperature in the axial direction and end effects ([2]). The heat flow becomes strictly radial. The steady-state radial temperature distribution $T(r)$ in a cylindrical domain with the constant thermal conductivity k, in which the heat is generated uniformly at a rate Q per unit volume, may be obtained from the following one-dimensional heat equation ([2])

$$\frac{d^2T(r)}{dr^2} + \frac{1}{r}\frac{dT(r)}{dr} - \frac{Q}{k} = 0 \quad . \tag{6.5}$$

The above equation can be derived from general heat equation (3.2) ([2], [13], [14]). The solution gives the steady-state temperature distribution at any point along a radius r. With the boundary condition $T(r_0)$ for $r = r_0$, where $T(r_0)$ is the temperature at the cylinder surface and r_0 is the radius of the cylinder, it follows that

$$T(r) = T(r_0) + \frac{Q}{4k}(r_0^2 - r^2) \quad . \tag{6.6}$$

The temperature profile is parabolic, with the highest temperature at the centre of the cylinder. The heat generated per unit volume can be expressed as

$$Q = \frac{P_h}{\pi {r_0}^2 L} \quad , \tag{6.7}$$

where L is the cylinder height and P_h is the total heat dissipated by the rod.

Rod

In the examined case of a rod we have assumed $P_h = 0.1\ W$ total heat dissipated in a rod with dimensions $L = 5\ cm$ and $r_0 = 0.5\ cm$ made of fused silica glass with constant thermal conductivity $k = 1.38\ W/(m \cdot K)$. We have assumed that the coolant flowing along the cylindrical rod surface guarantees constant temperature $T(r_0) = 293.15K$.
The steady-state radial temperature distribution $T(r)$ results in radial refractive index distribution $n(r)$ in the rod which may be for a fused silica glass expressed as follows ([25], assuming wavelength $1\mu m$)

$$n(r) = p_{T2}T(r)^2 + p_{T1}T(r) + p_{T0} \quad , \tag{6.8}$$

where $p_{T2} = 1.375 \cdot 10^{-8}\,[1/K^2]$, $p_{T1} = 6.644 \cdot 10^{-7}\,[1/K]$, $p_{T0} = 1.449\,[-]$. If we substitute for the temperature T from the expression (6.6) and expand we obtain

$$n(r) = p_{r4}r^4 + p_{r2}r^2 + p_{r0} \quad , \tag{6.9}$$

where

$$p_{r4} = p_{T2}\frac{Q^2}{16k^2} \quad \left[\frac{1}{m^4}\right] \tag{6.10}$$

$$p_{r2} = -p_{T2}\frac{Q^2 r_0^2}{8k^2} - p_{T1}\frac{Q}{4k} - p_{T2}\frac{QT(r_0)}{2k} \quad \left[\frac{1}{m^2}\right] \tag{6.11}$$

$$p_{r0} = p_{T2}\frac{Q^2 r_0^4}{16k^2} + p_{T1}\frac{Qr_0^2}{4k} + p_{T2}\frac{QT(r_0)r_0^2}{2k} + p_{T0} + p_{T1}T(r_0) + p_{T2}T(r_0)^2\,[-] \quad . \tag{6.12}$$

Both radial temperature and refractive index distribution are plotted in the figure 6.9. The

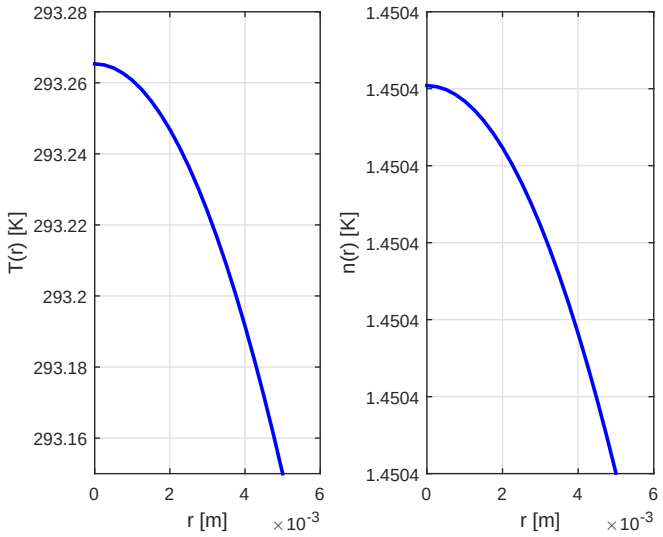

Figure 6.9: Radial temperature $T(r)$ and refractive index $n(r)$ distribution w. r. t. radial distance r in the rod, $z = L/2$.

radial refractive index distribution (6.9) is a forth order polynomial function. Obtaining the closed-form solution of the differential ray equation (3.12) would be quite tedious for this particular radial distribution, therefore it is advantageous to consider some simplifications. One approach to solve the differential equation (3.12) is to describe the ray trajectory by two functions $x(z)$ and $y(z)$, for the infinitesimal element of the arc length along the ray write $ds = \sqrt{1 + (dx/dz)^2 + (dy/dz)^2}$, and substitute into equation (3.12) to obtain two partial differential equations for $x(z)$ and $y(z)$. The paraxial approximation for which $ds \approx dz$ simplifies considerably the algebra of the solution ([4]). The equations (3.12) become

$$\frac{d}{dz}\left(n\frac{dx}{dz}\right) \approx \frac{\partial n}{\partial x} \tag{6.13}$$

$$\frac{d}{dz}\left(n\frac{dy}{dz}\right) \approx \frac{\partial n}{\partial y} \tag{6.14}$$

In the rod under consideration the refractive index $n = n(r)$ is constant in azimuthal φ and longitudinal z-direction and varies continuously only in the radial r-direction. The trajectories of paraxial rays in the r-z plane are described by the paraxial ray equation

$$\frac{d^2r}{dz^2} = \frac{1}{n}\frac{dn}{dr} \quad . \tag{6.15}$$

Given $n(r)$ and the initial conditions r and dr/dz at $z = 0$ equation (6.15) can be solved for the function $r(z)$, which describes the ray trajectories.
To simplify the solution even more, the radial distribution $n(r)$ expressed in (6.9) was re-fitted with a following function ([4])

$$n(r) = n_0(1 - \alpha^2 r^2)^{1/2} \quad , \tag{6.16}$$

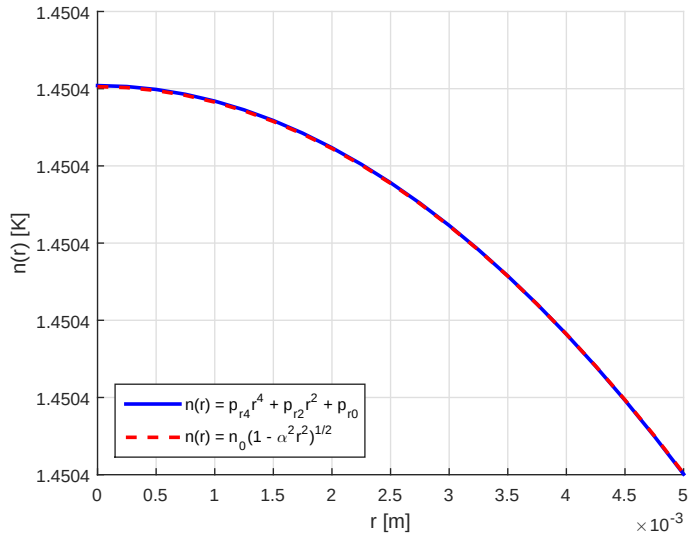

Figure 6.10: Comparison of refractive index $n(r)$ distributions (6.9) and (6.16), $z = L/2$.

where $n_0 = 1.45$ and $\alpha = 0.05526\ 1/m$ with a negligible RMSE error of $2 \cdot 10^{-12}$ (see figure 6.10 for comparison of refractive index distributions). Refractive index distribution (6.16) represents a widely used distribution known as SELFOC. The main advantage of switching to a SELFOC index distribution is that for $\alpha^2 r^2 << 1$ the distribution (6.16) may be approximated as a parabolic distribution

$$n(r) = n_0(1 - \frac{1}{2}\alpha^2 r^2) \quad . \tag{6.17}$$

Further, because $n(r) - n_0 << n_0$, the fractional change of the refractive index is very small. Taking the derivative of (6.17), the right-hand side of equation (6.15) is $1/n\ dn/dr = -(n_0/n)^2\alpha^2 r \approx -\alpha^2 r$, so that equation (6.15) becomes

$$\frac{d^2 r}{dz^2} = -\alpha^2 r \quad . \tag{6.18}$$

The solution of this differential equation are harmonic functions

$$r(z) = r_0 \cos \alpha z + \frac{\theta_0}{\alpha} \sin \alpha z \quad , \tag{6.19}$$

where $r_0 = r(0)$ and θ_0 is the initial slope dr/dz at $z = 0$.
The rod geometry with specified dimensions was created in COMSOL and meshed with

1. quadrilateral mesh consisting of 250 elements (10 x 25 elements in r-axis x z-axis direction),

2. triangular mesh consisting of the same number of elements 250 in order to compare the results.

Both mesh configurations were imported into MATLAB and together with $n(r)$ distribution specified according to (6.17) subjected to the ray tracing algorithm. We have considered $N_R = 5$ rays propagating from the points $[r_i, -1, 0]\,, i = 1, 2, \cdots, 5$, where $r_i =$

$\frac{r_0}{N_R+1}, \frac{2r_0}{N_R+1}, \cdots, \frac{N_R r_0}{N_R+1}$ resulting in 5 normal incident rays uniformly distributed along the radial distance r at $z = 0$. Resulting ray trajectories and with respectful mesh under consideration are depicted in figures 6.11 and 6.12. Because of relatively small induced refractive index gradient along the r-axis bending of the incident rays is not clearly visible in the presented figures. To further analyse the numerical solution we have compared it with the closed-form solution from equation (6.19). Comparison of analytical and numerical solutions for both considered meshes as well as the calculated absolute errors for respectful rays are depicted in the figure 6.13.

It is worth to remark a few aspects we may observe in the figure 6.13 with presented results.

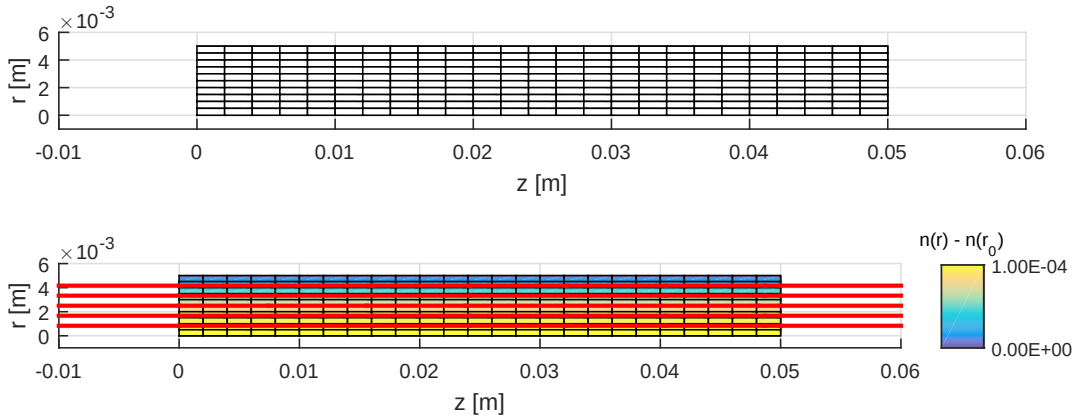

Figure 6.11: Resulting ray trajectories in thermally loaded axial symmetric glass rod. Quadrilateral mesh consisting of 250 elements.

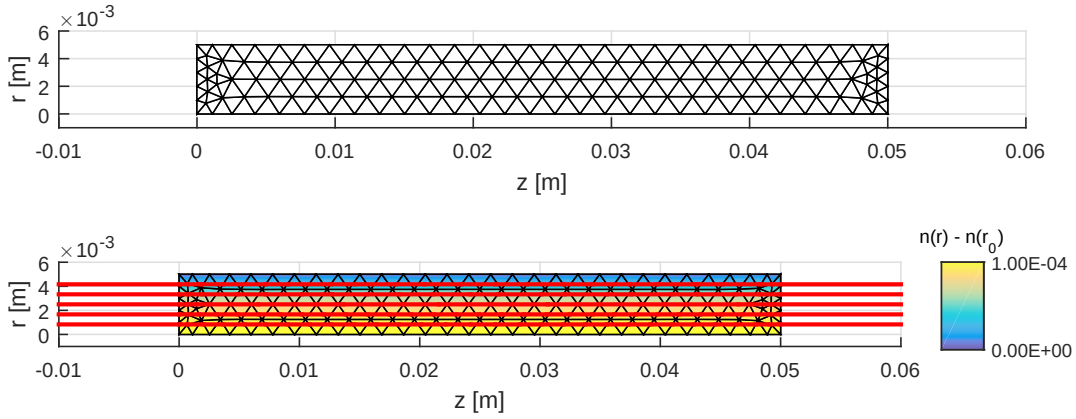

Figure 6.12: Resulting ray trajectories in thermally loaded axial symmetric glass rod. Triangular mesh consisting of 250 elements.

The absolute error apparently has an increasing trend as the rays propagates through a finite element discreticized medium. The resulting character of absolute error is exponential likewise and which is in good agreement with results presented in other papers ([19], [20],

[21]). The exponential growth of the error may generate relatively large errors for a thicker optical components and longer optical path lengths. This aspect should be always reminded when using the implemented ray tracing algorithm.
Further, it can be observed, that the absolute error is for all traced rays larger when the domain is discreticized with triangular elements. However, if we take a closer look at the meshes used in this particular case (figures 6.11 and 6.12) we may observe that in the r-axis direction the quadrilateral mesh consists of 10 layers of elements, whereas the tringular mesh the r-axis refractive index is approximated with only 4. This results in more poor approximation of radial gradient index field in the case of triangular mesh. Important observation which can be made here is that not only the total number, but also the shape of finite elements used for domain discretization greatly influences how accurate the gradient index field is approximated. For instance, extremely severe gradient fields should be discreticized with larger number of elements so that the gradient field is minimized across all the contained elements ([21]).
To acknowledge this theory the glass rod was remeshed with

1. quadrilateral mesh consisting larger number of elements - 7500 (150 x 50 elements in r-axis x z-axis direction),

2. triangular mesh consisting of the same number of elements 7500 with approximately the same number of layers 145 in r-axis direction as in the case of quadrilateral mesh.

Using the same radial refractive index distribution and set of rays the ray tracing was repeated. The resulting ray trajectories for more dense mesh along with the absolute error between analytical and numerical solutions are depicted in the figure 6.14. Note that the while the increasing trend remained the maximal error is now maintained within a few nanometers which is compared to the assumed wavelength of $1\mu m$ below 1%.

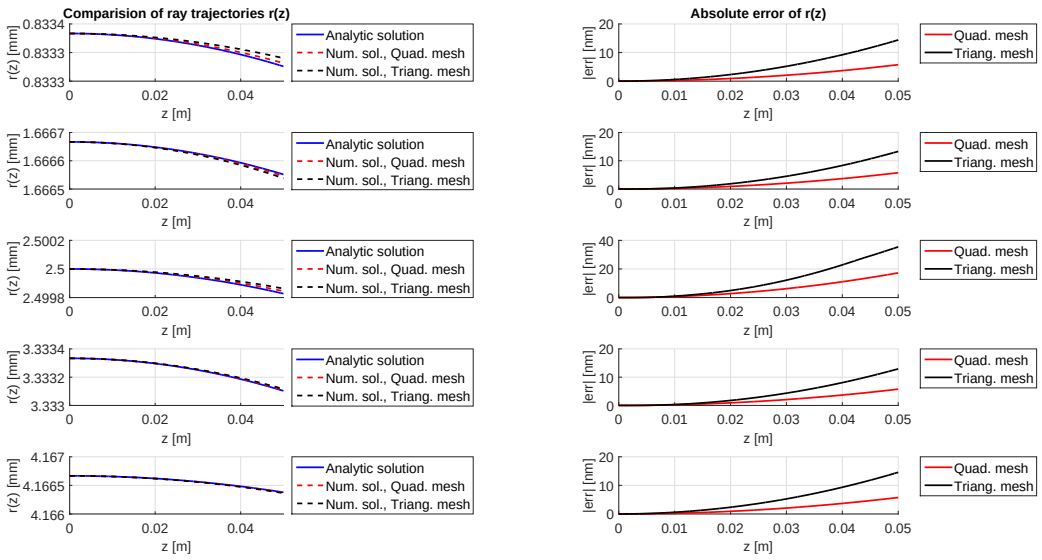

Figure 6.13: Comparison of analytical and numerical solutions for ray trajectories in thermally loaded axial symmetric glass rod. Both meshes consisted of 250 elements.

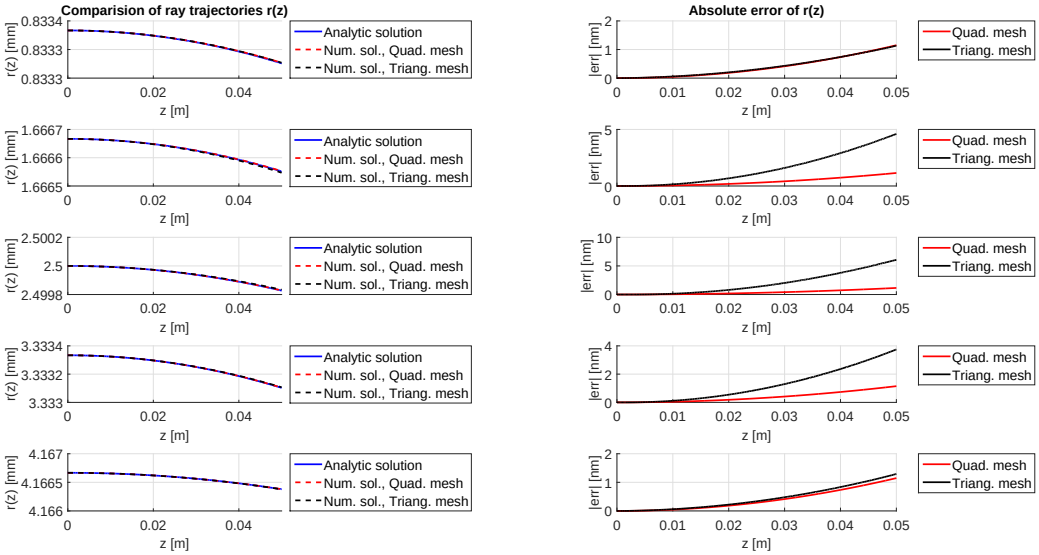

Figure 6.14: Comparison of analytical and numerical solutions for ray trajectories in thermally loaded axial symmetric glass rod. Both meshes consisted of 7500 elements.

Chapter 7

Ray tracing of a zigzag slab geometry

In the previous chapter the implemented ray tracing algorithm performance was validated in detail for both homogeneous and inhomogeneous refractive index media. The topic for a current chapter will be another possible usage of the implemented algorithm. We will investigate optical paths differences of a larger set of rays propagating in a optically pumped zigzag laser amplifier. A zigzag laser amplifier represents one of most widely used amplifier geometries. Simplified scheme in the figure 7.1 depicts the main idea of laser light amplification in an illustrative amplifier with zigzag geometry. The incident light is refracted on a skew boundary and propagates through the amplifier experiencing multiple total reflections. The goal of this procedure is to maximize the travelled distance of light through an active area experiencing amplification for a longer time. Compared to this illustrative scheme the geometric parameters as well as amplifier gain material differ according to the particular laser system.

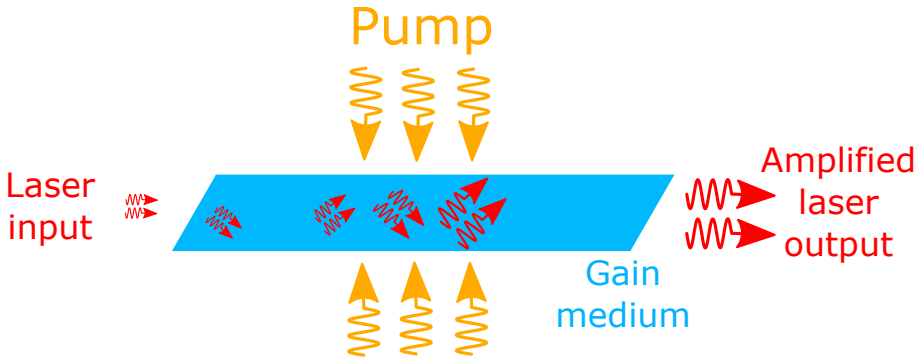

Figure 7.1: Simplified scheme of laser light amplification in an illustrative amplifier with zigzag geometry.

In our case a modification of zigzag laser amplifier presented in [26] will be considered. Compared to the article our considered zigzag amplifier will have different geometry parameters labeled according to the figure 7.2. The gain material is a commonly used laser crystal YAG (Yttrium Alluminium Garnet) doped with neodymium ions in central part of the amplifier with length L_{Nd} (see figure 7.2). The amplifier is optically pumped on both ends using radiation on wavelength 808 nm. The pump radiation is assumed to be absorbed only in

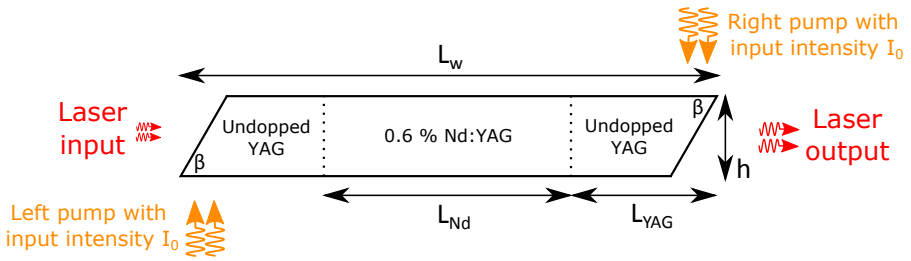

Figure 7.2: Zigzag amplifier geometry under consideration.

the active (dopped) area[1] according to a Beer-Lambert's law

$$I(x) = I_0 e^{-\alpha x} \quad , \tag{7.1}$$

where the intensity of the pump radiation $I(x)$ lowers exponentially with the distance travelled in x-axis direction. The parameter α denotes the absorption coefficient which is in general both wavelength and temperature dependent. In our case we will neglect the temperature dependence for the sake of simplicity. The heat load distribution results from Beer-Lambert's absorption of two counter-propagating pump radiations with equal input intensities I_0.
A two dimensional model of the zigzag amplifier with dimensions labelled according to the figure 7.2 was created in COMSOL environment. The specific values of geometry and simulation parameters are listed in table 7.1. Material properties of a YAG crystal were assumed to be constant with temperature (see table 7.2). A simplified heat removal scheme for the

Parameter	Value	Description
L_w	59.2 mm	slab length
L_{Nd}	33 mm	dopped area length
L_{YAG}	13.1 mm	undopped area length
h	10 mm	slab height
β	$\pi/4$ rad	angle of skew edges
h_0	4000 W/(m$^2 \cdot$ K)	heat transfer coefficient
P_0	100 W	pump source power
w_p	6 mm	pump square beam width
w_l	8 mm	laser square beam width
I_0	$6.66 \cdot 10^5$ W/m^2	input pump intensity
T_0	293.15 K	coolant temperature

Table 7.1: Simulation parameters.

thermo-mechanical simulations will be considered. Along the longer edges of the amplifier we will consider a convective heat flux q_0 boundary condition which may be expressed as

$$q_0 = h_0(T_0 - T), \tag{7.2}$$

where h_0 denotes the heat transfer coefficient and T_0 stands for the coolant temperature. The longer edges were also assumed to be fixed (non-deformable). The remaining skew edges

[1] Absorption of the pump radiation in the undopped part of the amplifier (pure YAG crystal) is compared to the absorption in the active area negligible.

Parameter	Value	Description
ρ	4.55 g/cm^3	density
C_p	590 J/(kg $\cdot$ K)	heat capacity at constant pressure
k	11.2 W/(m $\cdot$ K)	thermal conductivity
α_T	$6.14 \cdot 10^{-6}$ 1/K	thermal expansion coefficient
n_0	1.82	refractive index at initial temperature
dn/dT	$7.3 \cdot 10^{-6} \cdot 10^{-6}$ 1/K	thermo-optic coefficient for Nd:YAG (@1064 nm)
α	1.8 1/cm	absorption coefficient for Nd:YAG (@808 nm)

Table 7.2: Material properties of a YAG crystal ([26], [27]).

of the geometry are assumed to be thermally isolated and free to deform. Both quadrilateral and triangular mesh was generated for comparison reasons likewise to the simulations in the previous chapter dedicated to the algorithm validation.
The resulting temperature and displacement fields (see the figures 7.3 to 7.5) were along with the computational meshes imported into the MATLAB environment. For the ray tracing

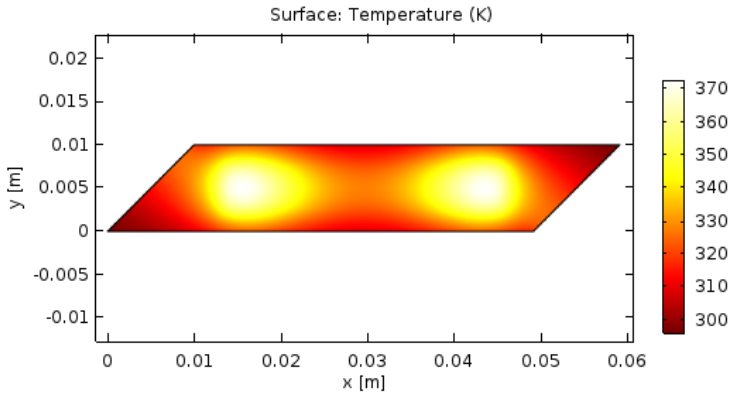

Figure 7.3: Zigzag amplifier temperature field.

algorithm we will consider 100 rays propagating in the x-axis direction defined as $[x_{ri}, y_{ri}, \alpha_{ri}]$, $i = 1, 2, \ldots, 100$, where $x_{ri} = -1$, y_{ri} is uniformly distributed in range $\langle \frac{h}{2} - \frac{w_l}{2}, \frac{h}{2} + \frac{w_l}{2} \rangle$ and $\alpha_{ri} = 0$. The ray trajectories were obtained for three different refractive index distributions within the domain.

1. Homogeneous constant refractive index field $n(x, y) = n_0$ to simulate the propagation in non-pumped amplifier.

2. Inhomogeneous refractive index field $n(x, y) = f(T(x, y))$ varying only with temperature $T(x, y)$ according to the equation (3.9).

3. Inhomogeneous refractive index field on deformed mesh $n(x, y) = g(T(x, y), d(x, y))$ where the refractive index $n(x, y)$ is dependent on both temperature $T(x, y)$ and displacement field $d(x, y)$.

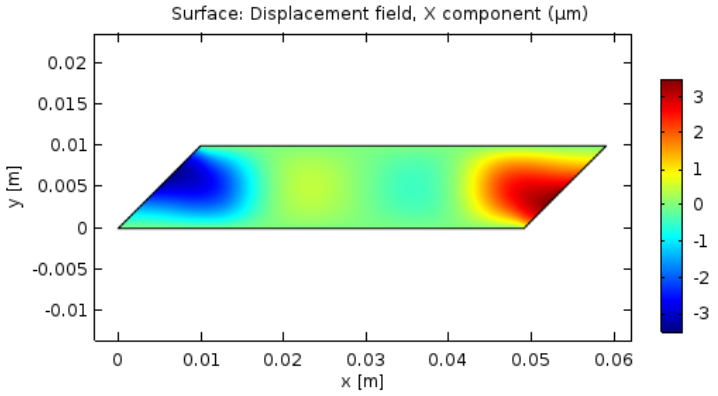

Figure 7.4: Zigzag amplifier displacement field, x-component.

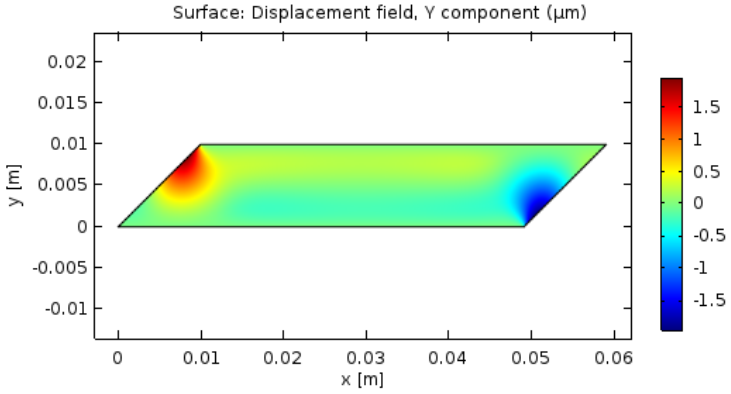

Figure 7.5: Zigzag amplifier displacement field, y-component.

Figures 7.6 and 7.7 shows the obtained trajectories for the first and second considered refractive index distribution[2].Only five out of a hundred trajectories were plotted to retain readability.
Optical paths defined according to the equation (3.13) were calculated for all obtained trajectories starting at the beginning point $[x_{ri}, y_{ri}, \alpha_{ri}]$ and ending at the point where the respectful ray intersect the vertical line at $x = 0.06\ m$ (right behind the amplifier). From the resulting optical paths the minimum value was subtracted in order to get the optical path difference which was then normalized to a laser emission wavelength of Nd:YAG 1064 nm. The optical path differences are plotted in the figure 7.8 with respect to the y-coordinate of the intersection of respectful output rays with the vertical line at $x = 0.06$.
The presented result is well demonstrating the influence of thermo-optic effects introduced in the third chapter. Notice that while the rays propagating through the non-pumped amplifier have travelled the same optical path, the rays propagated through the pump-heated amplifier have travelled each different optical path. Difference between the minimal and maximal optical path travelled reaches up to more than 2.5 multiple of the wavelength for the case where $n(x, y) = f(T(x, y))$ and more than 1.5 multiple of the wavelength for the case of $n(x, y) = g(T(x, y), d(x, y))$. This truly refers to thermal wavefront abberations

[2]Plot for the third considered case would be visually the same as the plot in the figure 7.7 since the deformations are of order 10^{-6}

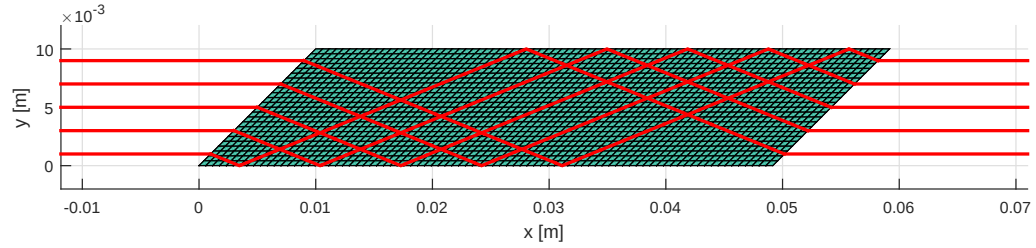

Figure 7.6: Obtained trajectories for the constant refractive index field within the modeled zigzag amplifier.

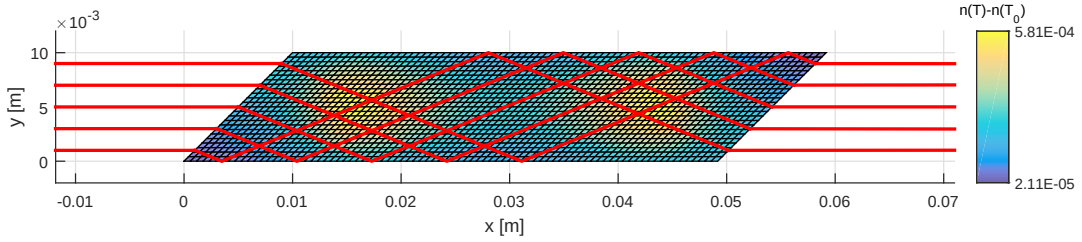

Figure 7.7: Obtained trajectories for the inhomogeneous refractive index field within the modeled zigzag amplifier.

which eventually cause output beam quality degradation (see again the thermo-optic effects scheme in the third chapter). The influence of considering the thermal deformation is also worth noting. Even a few micrometers deformed skew edges of the computational domain caused a slightly different shape of OPD. However, its magnitude is comparable to the case in which only the temperature dependent variation of refractive index was considered. With this observation we may refer to the earlier presented fact that the temperature dependent refractive index variation is often dominant compared to the stress dependent refractive index variation. This definitely holds also for our examined case of the zigzag amplifier, but for a different case (i. e. investigation of wavefront distortions in some thin optical components) neglecting the stress dependent refractive index variation would cause a large error in simulated results.

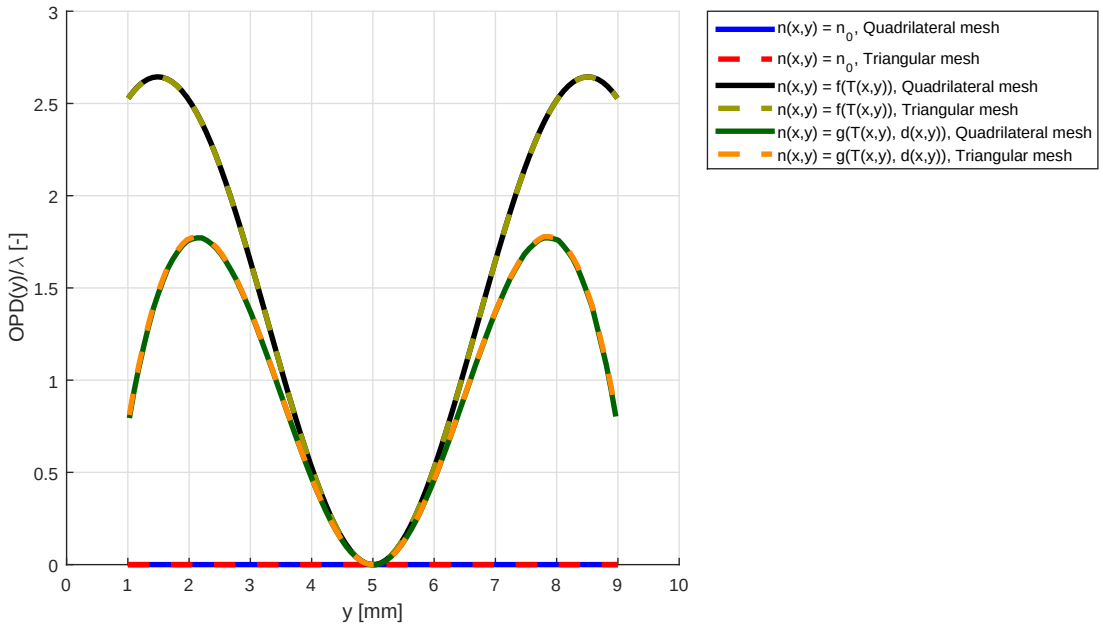

Figure 7.8: The resulting optical paths differences normalized by laser beam wavelength 1064 nm. Comparison of computational meshes.

Chapter 8

Conclusions and future work

This work deals with numerical simulations of a laser beam propagation through a thermally loaded solid-state media. The particular media of interest are commonly used optical components in solid-state laser systems. An operation of a laser system is always associated with thermo-optic effects arisen due to a parasitic power absorption in all optical components. Untreated thermal effects may result in output power loses, beam quality degradation, laser system destabilization and eventually even in a fracture of optical components. This becomes more serious problem especially in high-average-power laser systems. Therefore, a reduction of the thermal effects has to be considered during the system design. The core task of the thesis was to design and implement a numerical algorithm for simulation of a laser beam propagation in optical components commonly used in solid-state laser systems. The algorithm may be used in development process and for thermo-optic analysis of optical components. Within the work only two dimensional problems were considered and a laser beam was approximated as a set of rays.

In order to built the mathematical base for the algorithm the set of model equations used for thermo-optical analysis of an isotropic medium was presented in the third chapter. The set mainly consists of partial differential equations for which obtaining analytical solution is in most cases very tedious or even impossible. Therefore the finite element method was briefly introduced in following chapter as a tool to solve a set of PDEs. Main implementation steps were mentioned and more detailed insight into key concepts of FEM (2D meshing and linear shape functions) was given in the forth chapter.

The numerical algorithm was then built on the mathematical basis of FEM to enable numerical solving of differential ray equation within a general 2D discretized graded-index deformed medium.

The algorithm was implemented in MATLAB environment. Its performance was comprehensively validated on several illustrative simulation examples. The first examined case was the case of constant refractive index glass domain incident with a set of normal and oblique rays. The proper refraction on domain boundaries was verified.

More detailed investigation of refraction was done in simulation of a lens spherical abberations. In this case the numerical results were presented for focal point $f(h)$ varying with the ray intersection distance h from the optical axis. It has been shown that the numerical solution obtained for $f(h)$ approach to the presented thin lens analytical solution as the investigated lens becomes more thin. The obtained relative error of numerical solution was for the ratio between the lens thickness and radius of curvature $d/R = 0.004$ below 0.03 %.

The next simulation example was dedicated to algorithm validation for a graded-index media. Widely used axially symmetric rod geometry was considered assuming strictly radial refractive index variation as a result of parasitic heating. The thermal deformation were neglected for the sake of simplicity and only the temperature dependent variation of refractive index was considered. Numerical solutions for trajectories of 5 normal incident rays were presented and compared with the analytical solution of corresponding paraxial ray equation. It has been observed that the geometrical shape of disretizing elements as well as their total number influences greatly the accuracy of the numerical solution. In order to obtain more accurate solution, the computational mesh should be designed in such a way that the index gradients are almost constant within the finite element. This theory was confirmed by a repeated simulation with using mesh consisting of larger number of mesh elements. The absolute error of the numerical solution was in this case under 0.5% compared to the considered wavelength 1 μm of incident rays.
In the final chapter an illustrative case of calculation of optical path differences for a set of 100 rays propagating through a zigzag laser amplifier was presented. Three refractive index fields were considered within the simulation. 1) Constant, 2) Temperature varying only and 3) Temperature varying with thermal deformations of the medium included. The main goal was to show how the thermal effects strongly influence the output beam quality. The numerical results confirmed that while the rays propagating through the constant refractive index domain have travelled the same optical path, the rays propagating through the graded-index field have travelled each different optical path. Difference between the minimal and maximal optical path travelled reached up to more than 2.5 multiple of the considered wavelength for the case 2) and more than 1.5 multiple of considered wavelength for the case 3). This result suggest that in this case the stress dependent variation of refractive index is not compared to the temperature variation significant since the magnitude of obtained optical path differences is for both filds 2) and 3) comparable. However it should be reminded, that for a different case neglecting the stress dependent refractive index variation would cause a large error in simulated results. Such a case could be calculation of OPD for a very thin optical component.
No significant difference in terms of solution accuracy or computational efficiency was found between the triangular and quadrilateral computational meshes within this work. In all simulations in which both considered meshes were used the accuracy of obtained numerical solutions was comparable as well as the time of computation.
The next planned step for this work is extension of the algorithm into a 3D space enabling more advanced thermo-optic effects modelling. Apart from that, taking into account the material anisotropy is also a challenging.

References

[1] Vrbova, M., Jelinkova, H., and Gavrilov, P., *Uvod do laserove techniky*, Scriptum, CTU FNSPE, 1st edition (1998).

[2] Koechner, W., *Solid State Laser Engeneering*, Springer Science & Bussiness media, 6th edition, (2006).

[3] Born, M. and Wolf, E., *Principles of Optics*, 6th edition, (1980).

[4] Saleh, B. E. A. and Teich, M. C., *Fundamentals of Photonics*, John Wiley & Sons, 1st edition (1991).

[5] Engst, P., and Horak, M., *Aplikace laseru*, SNTL, 1st edition (1989).

[6] Koechner, W., *Thermal Lensing in a Nd:YAG Laser Rod*, Appl. Opt., Vol. 9, p. 2548-2553, (1970).

[7] Koechner, W. and Rice, D. K., *Effect of Birefringence on the Performance of Linearly Polarized YAG:Nd Lasers*, IEEE J. of Quant. El., Vol. 6, p. 557-566, (1970).

[8] Slezak, O., Lucianetti, A., Divoky, M., Sawicka, M. and Mocek, T., *Optimization of Wavefront Distortions and Thermal-Stress Induced Birefrengence in a Cryogenically-Cooled Multislab Laser Amplifier*, IEEE J. of Quant. El., Vol. 49, p. 960-966, (2013).

[9] Vojna, D., Slezak, O., Lucianetti, A. and Mocek, T., *Cooling options for high-average-power laser mirrors*, Proc. of SPIE, Vol. 9442, (2015).

[10] Kiriyama, H., Mori, M., Pirozhkov, A. S.; et al. *High-Contrast, High-Intensity Petawatt-Class Laser and Applications*, IEEE J. of Quant. El., Vol. 21, Iss. 1, (2015).

[11] Slezak, 0., Yasuhara, R., Lucianetti, A., Vojna, D. and Mocek, T., *Thermally induced depolarization in terbium gallium garnet ceramics rod with natural convection cooling*, J. of Opt., Vol. 17, Iss. 6, (2015).

[12] Novak, 0., Miura, T., Smrz, M.; et al. *Status of the High Average Power Diode-Pumped Solid State Laser Development at HiLASE*, App. Sciences-Basel, Vol. 5, p. 637-665, (2015).

[13] Ozisic, M. N., *Heat conduction*, John Wiley & Sons, 3rd edition, (2012).

[14] Boley, B. A. and Weiner, J. H., *Theory of thermal stress*, John Wiley & Sons, 3rd edition, (1993).

[15] Veselsky, K., *Thermal lens in solid-state laser active medium under low temperature*, Diploma Thesis, CTU FNSPE, (2015).

[16] Zienkiewicz, O. C. and Taylor, R. L., *The Finite Element Method: Its Basis and Fundamentals*, Elsevier, 6th edition, (2005).

[17] Rahman, B. M. A. and Agrawal, A., *Finite Element Modeling Method for Photonics*, Artech House, 2nd edition, (2013).

[18] Donea, J., Huerta, A., Ponthot, J. P., and Rodriguez-Ferran, *Arbitrary Lagrangian Eulerian Methods*, John Wiley & Sons, chap. 14 of *Encyclopedia of Computational Mechanics*, Vol. 1, *Fundamentals*, (2004).

[19] Sharma, A., Kumar, D. V. and Ghatak, A. K., *Tracing rays through graded-index media: a new method*, Appl. Opt., Vol. 29, p. 984 - 987, (1982).

[20] Richerzhagen, B., *Finite element ray tracing: a new method for ray tracing in a gradient index medium*, Appl. Opt., Vol. 35, p. 6186-6189, (1996).

[21] Shrader, K. N., Subia, S. R., Myre, J. W. and Summers, K. L., *Ray tracing in a finite-element domain using nodal basis functions*, Appl. Opt., Vol. 53, p. F10-F20, (2014).

[22] Press, W. H., Teukolsky, S. A., Vetterling, W. T. and Flannery, B. P., *Numerical recipes in C - The Art of Scientific Computing*, Cambridge University Press, 2nd edition, (1992).

[23] Mahajan, V. N., *Aberration Theory Made Simple*, SPIE Press, 1st edition, (1991).

[24] Smith, T. T., *Spherical Aberration in Thin Lenses*, Phys. Rev., Vol. 19, p. 276-277 (1922).

[25] Levinton, D. B., Frey, J. B., *Temperature-dependent absolute refractive index measurements of synthetic fused silica*, Proc. SPIE, Conf. Vol. 6273, (2006).

[26] Sridharan, A. K., Saraf, S., Sinha, S. and Byer, R. L., *Zigzag slabs for solid-state laser amplifiers: batch fabrication and parasitic oscillation suppression*, Appl. Opt., Vol. 45, p. 3340-3351, (2006).

[27] Aggarwal, R. L., Ripin, D. J., Ochoa, J. R. and Fan, T. Y. *Measurement of thermo-optic properties of* $Y_3Al_5O_{12}$, $Lu_3Al_5O_{12}$, $YAlO_3$, $LiYF_4$, $LiLuF_4$, BaY_2F_8, $KGd(WO_4)_2$ *and* $KY(WO_4)_2$ *laser crystals in the* 80-300 *K temperature range*, J. of Appl. Phys., Vol. 98, 103514, (2005).

[28] Kolukula, S. S., *Postprocessing in FEM*, `http://www.mathworks.com/matlabcentral/fileexchange/32719-postprocessing-in-fem`, (2011).

[29] Legland, D., *2D Geometry*, `http://www.mathworks.com/matlabcentral/fileexchange/7844-geom2d`, (2015).

[30] Dunlavy, D. M., Kolda, T. G. and Acar, E., *Poblano v1.0: A Matlab Toolbox for Gradient-Based Optimization*, Sandia National Laboratories, Albuquerque, NM and Livermore, CA, (2010).

List of Figures

Author's relevant publications

1. Vojna, D., Slezak, O., Lucianetti, A.; et al. *Cooling options for high-average-power laser mirrors*, Proc. of SPIE, Vol. 9442, (2015).

2. Kiriyama, H., Mori, M., Pirozhkov, A. S.; et al. *High-Contrast, High-Intensity Petawatt-Class Laser and Applications*, IEEE J. of Quant. El., Vol. 21, Iss. 1, (2015).

3. Kiriyama, H., Mori, M., Pirozhkov, A. S.; et al. *Recent Advances on the J-KAREN laser upgrade*, Conference on Lasers and Electro-Optics, (2015).

4. Slezak, 0., Yasuhara, R., Lucianetti, A.; et al. *Thermally induced depolarization in terbium gallium garnet ceramics rod with natural convection cooling*, J. of Opt., Vol. 17, Iss. 6, (2015).

5. Novak, 0., Miura, T., Smrz, M.; et al. *Status of the High Average Power Diode-Pumped Solid State Laser Development at HiLASE*, App. Sciences-Basel, Vol. 5, p. 637-665, (2015).

The contents of attached CD

In table 8.1 are listed names of all root files and directories on enclosed CD.

Directory or File name	**Description**
Analytical models and comparison	MATLAB scripts, functions and data used for comparison of analytical and numerical solutions.
Computational meshes	Computational meshes exported from COMSOL
COMSOL thermo-mechanical results	COMSOL thermo-mechanical results used within the work.
External MATLAB scripts and functions	Freely available MATLAB functions which modified version was used in the algorithm ([28] - [30]).
Ray tracing algorithm	Developed and modified MATLAB scripts, functions and data for the ray tracing algorithm.
DP_Vojna_David_2016.pdf	PDF-form diploma thesis.

Table 8.1: The contents of the CD.